



HAL
open science

Holocene dynamics of the southern westerly winds over the Indian Ocean inferred from a peat dust deposition record

Chuxian Li, Jeroen E. Sonke, Gaël Le Roux, Nathalie van Der Putten, Natalia Piotrowska, Catherine Jeandel, Nadine Mattielli, Mathieu Benoit, Giles F.S. Wiggs, François de Vleeschouwer

► To cite this version:

Chuxian Li, Jeroen E. Sonke, Gaël Le Roux, Nathalie van Der Putten, Natalia Piotrowska, et al.. Holocene dynamics of the southern westerly winds over the Indian Ocean inferred from a peat dust deposition record. *Quaternary Science Reviews*, 2020, 231, pp.106169. 10.1016/j.quascirev.2020.106169 . hal-02895456

HAL Id: hal-02895456

<https://hal.science/hal-02895456>

Submitted on 16 Nov 2020

HAL is a multi-disciplinary open access archive for the deposit and dissemination of scientific research documents, whether they are published or not. The documents may come from teaching and research institutions in France or abroad, or from public or private research centers.

L'archive ouverte pluridisciplinaire **HAL**, est destinée au dépôt et à la diffusion de documents scientifiques de niveau recherche, publiés ou non, émanant des établissements d'enseignement et de recherche français ou étrangers, des laboratoires publics ou privés.

1 Holocene dynamics of the southern westerly winds over the Indian
2 Ocean inferred from a peat dust deposition record

3 Chuxian Li^{1,2*}, Jeroen E. Sonke², Gaël Le Roux¹, Nathalie Van der Putten³, Natalia Piotrowska⁴,
4 Catherine Jeandel⁵, Nadine Mattielli⁶, Mathieu Benoit², Giles F.S. Wiggs⁷, François De
5 Vleeschouwer^{1**}

6
7 1. EcoLab, Université de Toulouse, CNRS, INPT, UPS, Toulouse, France.

8 2. Laboratoire Géosciences Environnement Toulouse, Université de Toulouse, CNRS, IRD, UPS, Toulouse, France.

9 3. Faculty of Science, Earth Sciences, Cluster Earth and Climate, Vrije Universiteit Amsterdam, the Netherlands.

10 4. Silesian University of Technology, Institute of Physics-CSE, Gliwice, Poland.

11 5. LEGOS Université de Toulouse, CNRS, CNES, IRD, UPS, Toulouse, France.

12 6. Laboratoire G-Time, DGES, Université Libre de Bruxelles (ULB), Belgium.

13 7. School of Geography and the Environment, Oxford University Centre for the Environment, University of Oxford,
14 South Parks Road, Oxford,OX1 3QY, United Kingdom.

15 * Corresponding author, chuxian.li@ensat.fr

16 At: EcoLab / Campus Ensats, Avenue de l'Agrobiopole, 31326 Castanet-Tolosan, France

17 ** Present address: Instituto Franco-Argentino para el Estudio del Clima y sus Impactos (UMI 3351 IFAECI/CNRS-
18 CONICET-UBA), Universidad de Buenos Aires, Argentina

19

20

21 **Abstract:**

22 The southern westerly winds (SWW) play a major role in climate variability in Southern
23 Hemisphere mid- and high- latitudes, regulating rainfall, ocean circulation, and the Southern
24 Ocean carbon sink. Despite their importance, little is known about millennial scale changes in
25 the SWW and how they have influenced the climate system in the past and interacted with the
26 Earth's surface elements, such as dust, nutrients and carbon. Here we present a dust record
27 from a 6.6 kyr old peat core in Amsterdam Island (AMS) situated at the northern edge of the
28 SWW (37°S) in the Southern Indian Ocean. Mineral dust flux was used to track atmospheric dust
29 production, long-distance transport and subsequent deposition. Dust provenance was
30 determined from rare earth element (REE) and Nd isotopic signatures (ϵNd) in the core,
31 compared with a reference dataset of Southern Hemisphere dust sources. Using a multi-proxy
32 mixing model, the ϵNd and REE ratios show a relatively uniform mixture of ca. 40% local, 15%
33 Southern African and 45% Southern South American dust sources since 6.6 cal. kyr BP. However,
34 from 1910 AD onwards, there is a doubling in the contribution from Southern Africa (32%). Two
35 mineral dust flux minima occur at 6.2 - 4.9 cal. kyr BP and 3.9 - 2.7 cal. kyr BP, interpreted as
36 periods with equatorward-shifted and/or strengthened SWW at the northern edge of the wind
37 belts. Conversely, periods of higher dust flux at 6.6 - 6.2 cal. kyr BP, 4.9 - 3.9 cal. kyr BP, and 1.4
38 cal. kyr BP onwards are interpreted as poleward-shifted and/or weakened SWW. These
39 interpretations are based on the findings that higher (lower) wind speeds lead to enhanced (less)
40 removal of distal dust on the way to AMS, by wet deposition and turbulence. Published
41 Holocene SWW records at the northern edge of the wind belt (33 - 41°S) covering South-
42 America, Southern-Africa and Australia, show much variability over the last 6.6 kyr. We suggest

43 this reflects complex regional climate variability of the SWW in the different SH longitudinal
44 sectors, indicating that SWW are not zonally homogeneous at the northern edge of the wind
45 belts. The recent shift in dust provenance is not accompanied by enhanced total dust deposition
46 at AMS. We therefore suggest that human impact (e.g., land use changes) and drier climate
47 conditions in Southern Africa have led to enhanced dust mobilization.

48 **Keywords:** southern westerly winds; dust sources; peat; Amsterdam Island; anthropogenic
49 activities.

50

51 **1. Introduction**

52 The strength and position of the southern westerly winds (SWW) vary seasonally due to
53 changes in the sea surface temperature (Lamy et al., 2010). SWW shift equatorward and expand
54 during the austral winter, while they move poleward and contract during the austral summer.
55 Latitudinal displacement in annual-mean SWW position can be affected by both external factors
56 (e.g., long-term orbital forced insolation changes, Varma et al., 2012, 2011), and internal factors
57 (e.g., Southern Annual Mode changes, Gillett and Thompson, 2003). Changes in the annual-
58 mean strength and position of SWW play a major role in climate variability of SH mid- and high
59 latitudes (e.g., affecting precipitation pattern, Jenny et al., 2003). The SWW are also an
60 important driver of ocean circulation, nutrient transport and the global carbon cycle (Kohfeld et
61 al., 2013). Around 40% of anthropogenic CO₂ emissions are currently taken up by the Southern
62 Ocean south of 35°S (Frölicher et al., 2015; Landschützer et al., 2015; Sabine et al, 2004). It has
63 been suggested that poleward-shifts and intensification of the SWW can enhance upwelling of
64 deep water with high concentrations of dissolved inorganic carbon, limiting the capacity of the
65 ocean to absorb carbon at the surface, resulting in additional global warming (Denton et al.,
66 2010; Hodgson and Sime, 2010; Lovenduski et al., 2008) .

67
68 An increase in SWW strength has been observed in recent decades (e.g., Hande et al., 2012;
69 Marshall et al., 2006; Thompson and Solomon, 2002). Swart and Fyfe (2012) suggest that under
70 high CO₂ emission scenarios, the SWW could shift up to 1.5° southwards and strengthen by up
71 to 10% by the end of the 21st century (relative to the current annual-mean SWW position and
72 strength). These changes will have significant environmental and climatic implications (Zickfeld

73 et al., 2007). To understand the influence of SWW on Earth's climate requires a better
74 knowledge of the interactions between SWW dynamics and climate in the past, especially in the
75 Holocene (Fletcher and Moreno, 2012).

76
77 Up to now, a range of direct and indirect proxies in different stratigraphic archives (e.g., peat
78 and sediment cores) have been used to reconstruct Holocene SWW fluctuations (e.g., Lamy et
79 al., 2010; Moreno et al., 2010; Saunders et al., 2018, 2012; Van der Putten et al., 2008).
80 However, no consensus has been reached on past intensity and/or latitudinal changes of the
81 SWW at the whole wind belts. Some studies argue for a strengthening/equatorward shift of the
82 SWW during the mid-Holocene (ca. 7 - 4 cal. kyr BP) relative to the early Holocene (ca. 11 - 7 cal.
83 kyr BP) based on studies from Southern Africa (Fitchett et al., 2017; Humphries et al., 2017) ,
84 Southern South America (Jenny et al., 2003; Moreno et al., 2010) , Australia and New Zealand
85 (Shulmeister, 1999). Other studies suggest a poleward displacement of the SWW during the
86 same period resulting in a decreased westerly influence in Southern Africa (Chase et al., 2013),
87 Southern South America (Frugone-Álvarez et al., 2017; Lamy et al., 2010, 2001), Australia and
88 New Zealand (Marx et al., 2011). These studies are mainly conducted on the continents, which
89 are under the combined influence of SWW and other regional climate and orographic factors
90 (e.g., the monsoon system in Australia and the presence of the Andes in South America).

91
92 Relatively few paleoclimatic studies (Lindvall et al., 2011; Ljung and Björck, 2007; Saunders et
93 al., 2018, 2012; Van der Putten et al., 2012, 2008), have attempted to reconstruct Holocene
94 SWW variability from oceanic islands where these factors are largely absent. Currently there are

95 no SWW reconstructions at the northern edge of the SWW belt in the southern Indian Ocean.
96 We address this by studying the Holocene mineral dust flux and its composition in peat profiles
97 in Amsterdam Island (37°S). Mineral dust flux is a function of both changes in dust provenance,
98 wind transport and deposition (Vanneste et al., 2015). Specifically, dust flux is a function of
99 environmental factors, including aridity and air mass circulation over source areas (Marx et al.,
100 2009; Thompson et al., 2002), dust atmospheric residence time (Betzer et al., 1988), as well as
101 the strength and trajectories of transporting winds (Kohfeld et al., 2013). Changes in dust flux
102 can be seen in the variabilities of geochemical and isotopic compositions (e.g., rare earth
103 elements (REE) and Neodymium (Nd) isotopes, Vanneste et al., 2016, 2015). Amsterdam Island
104 is remote and nearly free from human disturbance, which makes it an ideal location to measure
105 dust flux and provenance, and determine past changes in wind dynamics (Gaudichet et al.,
106 1989).

107
108 The specific objectives of this study were to: (1) investigate the dust flux in peat core from
109 Amsterdam Island; (2) identify the provenance of the dust by comparing core samples with a
110 reference dataset of dust geochemistry and isotopic signatures from the Southern Hemisphere;
111 (3) interpret these measurements in terms of past changes in the dynamics of the SWW at their
112 northern limit in the Indian ocean, through comparison with other Southern Hemisphere (SH)
113 records; and (4) probe the anthropogenic impact on the Southern Hemisphere based on the
114 dust variability in Amsterdam Island peat core. This study can also provide an observational
115 dataset for climate model parameterizations, especially in terms of the future impact of changes
116 in the SWW on continental rainfall and the global carbon cycle.

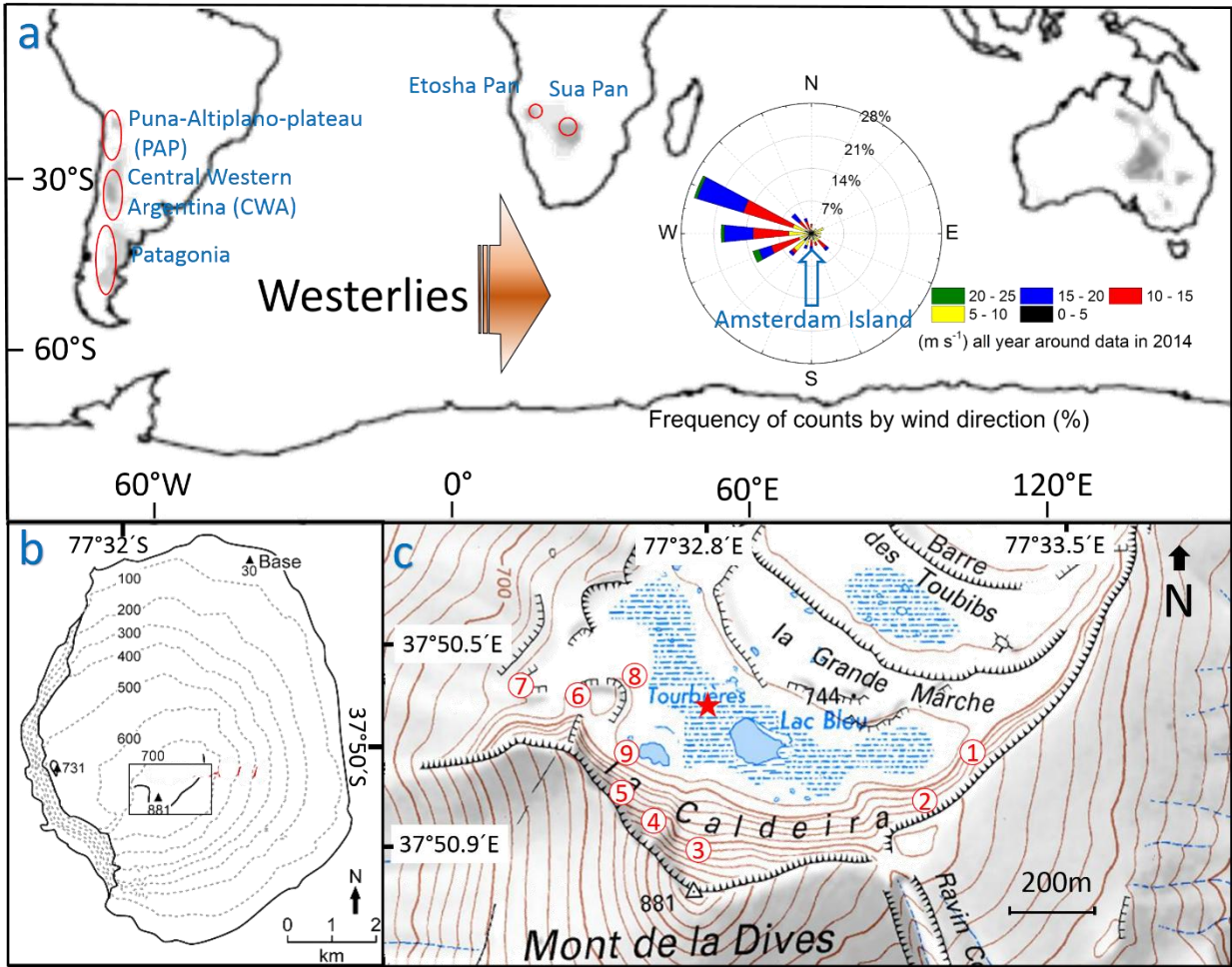
117

118 **2. Material and Methods**

119 **2.1. Site description**

120 Amsterdam Island (AMS, 37°50'S, 77°32'E) is a small (55 km²) isolated volcanic island located
121 4200 km to the east of South Africa and 3200 km to the west of Australia (Fig. 1a, b). The island
122 has steep cliffs along its western coast rising to a central caldera at 720 m above sea level (a.s.l.,
123 Flatberg et al., 2011; Doucet et al., 2003) (Fig. 1c). The highest point is Mont de La Dives at 881
124 m a.s.l. AMS is currently at the northern edge of the SWW belt, and just north of the oceanic
125 subtropical front (Orsi et al., 1995). It has a mild oceanic climate with frequent cloud formation
126 at the caldera. Mean annual temperature at the meteorological station (27 m a.s.l.) is 14°C and
127 annual precipitation is about 1100 mm (De Vleeschouwer et al., 2014; Lebouvier and Frenot,
128 2007). The wind strength is 7.4 m s⁻¹ on average (Météo France data reported in Frenot and
129 Valleix, 1990). However, climate conditions on the central plateau are harsher with a mean
130 annual temperature of 7°C and twice as much rainfall (Frenot and Valleix, 1990). The soil around
131 the central plateau is poorly developed and consists of water-saturated sandy loams developed
132 to a maximum depth of 60 cm (Frenot and Valleix, 1990). The wetter conditions at higher
133 altitudes of the island (above 500 m a.s.l.) favor moss growth (e.g., *Sphagnum* mosses) and peat
134 accumulation, in particular on the central plateau (Flatberg et al., 2011).

135



136

137 Fig. 1. Sampling sites on Amsterdam Island (AMS) and in the potential dust source areas in the Southern
 138 Hemisphere. (a) The core of the wind rose represents the location of Amsterdam Island. Wind rose data are
 139 courtesy of the Institut de Géosciences et de l'Environnement in Grenoble, France. The orange arrow
 140 represents Southern Westerly winds (SWW), whose core currently centers at 50-55°S (Saunder et al., 2018).
 141 The grey areas shown in Southern South America and Southern Africa, represents days per months (darker =
 142 more days) with dust activity (modified after Prospero et al., 2002). Red ellipses are soil sampling areas at
 143 Puna-Altiplano-Plateau, Central Western Argentina and Patagonia in Southern America (data from Gili et al.,
 144 2017); and dust/soil sampling sites at Sua Pan and Etosha Pan in Southern Africa. (b) Map of AMS. The black
 145 rectangle has been enlarged in Fig. c. (c) Locations of the peat coring site AMS14-PB01A (red star) and soil
 146 sampling sites (numbers shown in red) at AMS.

147

148 2.2. Sample collection and preparation

149

A 5 m-long peat sequence (AMS14-PB01A, 37°50.742'S, 77°32.898'E, Fig.1c) was collected
 150 from the center of the caldera peatland at 738 m a.s.l. (Fig. 1; Fig. S1) in December 2014 using a
 151 50 cm long Russian corer with an internal diameter of 10 cm (Belokopytov and Beresnevich 1955;

152 De Vleeschouwer et al., 2014). Two further cores (AMS14-PB01B, 4.15 m length; AMS14-PB01C,
153 top 1 m length) were collected and archived. Cores were photographed, described, wrapped in
154 plastic film and PVC tubes, and shipped to France refrigerated at +4 °C. Cores were frozen and
155 subsequently sliced at roughly 1-cm resolution using the sub-sampling procedure described in
156 De Vleeschouwer et al., (2010) and Givelet et al., (2004).

157

158 To study the chemical and isotopic provenance of dust in the core, we assembled a reference
159 dataset consisting of nine top soil samples from this island, representative of local dust sources
160 (Fig. 1c), together with samples from the two major SH dust sources (Fig. 1a). These were
161 identified from observational and modelling data (Bryant et al., 2007; Engelstaedter and
162 Washington, 2007; Prospero et al., 2002; Vickery et al., 2013) and include: (1) Botswana and
163 Namibia in Southern Africa; and (2) the Altiplano, Western Argentina and Patagonia in Southern
164 South America. Australia is not considered as an important distal dust source for AMS because
165 limited air masses originate from Australia according to the 14-day Hysplit back trajectory
166 ensembles at AMS (Fig. S2, Text S1) and most Australian dust is transported eastward to the
167 Pacific Ocean (Li et al., 2008). Chemical analysis on AMS also supports minimal present
168 Australian dust contribution to AMS (Gaudichet et al., 1989). Specific reference dust/soil
169 samples in this study were collected from (1) local; (2) Sua Pan (Botswana) and (3) Etosha Pan
170 (Namibia) in Southern Africa (Fig. 1a, c). More information on Southern African dust/soil and
171 local AMS soil are given in the supplementary information Text S2, Table S1 and Table S2,
172 respectively. Dataset of Southern American surface sediments (including Puna-Altiplano-Plateau,
173 Central Western Argentina and Patagonia) are from Gili et al., (2017).

174 **2.3. Analyses and methods**

175 **2.3.1. Radiocarbon dating and age model reconstruction**

176 Twenty peat samples were submitted for radiocarbon dating. Where possible monospecific
177 terrestrial plant remains (brown mosses or *Sphagnum* mosses) were dated, and where there
178 was insufficient material, both taxa were combined. Eleven of the radiocarbon samples were
179 pre-treated and graphitized at the GADAM center (Gliwice, Poland, GdA code) (Piotrowska, 2013)
180 and their ^{14}C concentration in graphite measured at the DirectAMS Laboratory (Bothell, WA,
181 USA). The NIST Oxalic Acid II standard was used for normalization, and black coal was used as a
182 blank. The other nine radiocarbon samples were pre-treated, graphitized and dated at
183 Plateforme Nationale LMC14 (CNRS-CEA Saclay, France, SacA code). Normalization of the
184 measurements at LMC14 Laboratory was done with Oxalic Acid 1 standard. Blanks were
185 carbonate and charcoal (for details see Delqué-Količ et al., 2013; Moreau et al., 2013).

186
187 The surface of the core was dated with ^{210}Pb using the Constant Rate Supply model (Appleby,
188 2001), together with four post-bomb radiocarbon dates (Goodsite et al., 2001; Hua, 2009). The
189 ^{210}Pb Constant Rate Supply model has been validated by ^{137}Cs and ^{241}Am measurements (See Li
190 et al., 2017 for details). An age-depth model was generated from a combination of radiocarbon
191 dating, post-bomb and ^{210}Pb dating with the Bacon package version 2.2 updated in 2018
192 (Blaauw and Christen, 2011) within R software version 3.5 (R development Core Team, 2013)
193 using the SHCal13 calibration curve (Hogg et al., 2013). For modelling, the core was divided into
194 101 sections. The prior settings were default 10 year/cm for accumulation rate (gamma

195 distribution with shape 1.5), and memory was described by beta distribution with mem.strength
196 = 4 and mem.mean = 0.7. The median modelled age was used for plotting the data against time.

197

198 **2.3.2. Bulk density and ash content**

199 The density (g m^{-3}) of 377 samples was obtained by measuring the volume of each sample,
200 using a Vernier caliper, and weighing it after freeze-drying using an ALPHA 1e4 LD plus freeze-
201 dryer. The ash content was determined as the weight difference before and after ashing the
202 bulk peat samples in a furnace at 550°C for 5h.

203

204 **2.3.3. Major and trace element analyses**

205 We selected 101 freeze-dried AMS peat samples for elemental analysis based on the bulk
206 density results. 100 mg of each selected peat samples was used and 50 mg of each reference
207 soil/dust samples was used. These samples were digested in Teflon vials on a hot plate using an
208 HNO_3 -HF mixture (method modified from Vanneste et al., 2015, see supplementary information
209 Table S3 for more details). Subsequently, concentrations of Al, Ti, K and Sr were determined by
210 ICP-OES (IRIS Intrepid II) at Ecolab (Toulouse, France). Concentrations of trace elements (REE, Ga,
211 Hf, Zr, Th, U, Cs, Rb, Pb), Mg and Ca were measured by quadrupole ICP-MS (Agilent Technologies
212 7500ce) at the *Observatoire Midi-Pyrénées* (Toulouse, France).

213

214 Synthetic multi-element calibration solutions were used to calibrate the ICP-OES and ICP-MS
215 instruments. In addition, In-Re was added to both the ICP-MS calibration solutions and samples
216 as an internal standard. Several certified reference materials (CRMs) were used for quality

217 control: (1) NJV942 (*Sphagnum* peat, Swedish University of Agricultural Sciences, Sweden);
218 (2)NJV941 (*Carex* peat, Swedish University of Agricultural Sciences, Sweden); (3) SRM1515
219 (Apple leaves, NIST, US); (4) SRM1547 (Peach leaves, NIST, US); (5) LKSD-3 (lake sediment,
220 CANMET Mining and Mineral Sciences Laboratories, Canada); and (6) WQB-1 (lake sediment,
221 National Water Research Institute, USA). For further details on the quality control and quality
222 assurance see supplementary information Text S3, Table S4 and Table S4bis.

223

224 **2.3.4. Neodymium isotope analyses**

225 43 freeze-dried samples from the AMS peat core, and reference soil samples from AMS (nine
226 samples), Sua Pan (three soil and three dust samples), and Etosha Pan (three soil and three dust
227 samples), were selected for Nd isotope analysis. The weight of the peat samples (160 mg - 950
228 mg) and soil/dust samples (68 mg - 275 mg) required for the analyses was based on their Nd
229 concentrations and the sensitivity of the mass spectrometer. Before being digested in a mixture
230 of concentrated HNO₃ and HF, samples were ashed in a furnace at 550°C for 5h (Vanneste et al.,
231 2015). Subsequently, Nd was separated from the matrix within the sample solution using a two-
232 column ion exchange technique. The Nd isotope composition of all the samples was determined
233 by Thermal Ionization Mass Spectrometry (TRITON™ Plus) at the *Observatoire Midi-Pyrénées*
234 (Toulouse, France). Chemical blanks for Nd isotopic measurements were below the detection
235 limit. The Nd standards Rennes (¹⁴³Nd/¹⁴⁴Nd = 0.511973) and La Jolla (¹⁴³Nd/¹⁴⁴Nd = 0.511858)
236 were analyzed at every session to monitor instrumental drift. Measured values of La Jolla were
237 0.511844 ± 0.000012 (n=9) and of Rennes were 0.511956 ± 0.000006 (n=22). The three
238 replicated samples gave consistent ¹⁴³Nd/¹⁴⁴Nd values within the error bars.

239

240 The Nd isotopic signatures, expressed in ϵNd notation are calculated by the equation (1).

241
$$\epsilon\text{Nd} = \left(\frac{\left(\frac{^{143}\text{Nd}}{^{144}\text{Nd}}\right)_{\text{Sample}}}{\left(\frac{^{143}\text{Nd}}{^{144}\text{Nd}}\right)_{\text{CHUR}}} - 1 \right) \times 10^4 \quad (\text{Eq.1})$$

242 where CHUR is Chondritic Uniform Reservoir, representing a present day average earth value

243 $\left(\frac{^{143}\text{Nd}}{^{144}\text{Nd}}\right)_{\text{CHUR}} = 0.512638$ (Jacobsen and Wasserburg, 1980). ϵNd represents the deviation of

244 $^{143}\text{Nd}/^{144}\text{Nd}$ in a sample from the value in CHUR.

245

246 **2.4. Statistical methods**

247 A principal component analysis (PCA) was performed on all the elemental data (REE, Mg, Ca,

248 Ga, Rb, Zr, Cs, Hf, Th, U, Al, Pb, Ti, K, Sr) using the ‘psych’ package (Revelle, 2019) within R

249 software (R Development Core Team, 2013). Each principal component groups a set of elements

250 with similar variations along the peat profile. A varimax rotation is also performed for

251 maximizing the variances of the squared loadings in the components in order to facilitate the

252 interpretation (Abdi and Williams, 2010; Vanneste et al., 2016).

253

254 Change point analysis was performed with the Change-Point Analyzer 2.0 software (Taylor

255 Enterprises Inc., IL, <http://www.variation.com>) to identify significant shifts in the key proxies

256 through the Holocene (e.g., Castino et al., 2016; Killick et al., 2010; Reid et al., 2016) . The

257 method (Taylor, 2000a) is based on the mean-shift model under the procedure of a combination

258 of time-series cumulative sum charts and bootstrapping to detect change. The cumulative sums

259 are the cumulative sums of differences between the values and the average (for details on the

260 method see Taylor, 2000a; 2000b). The cumulative sum chart is optimal at detecting shifts in the

261 mean (Taylor, 2000a). 10,000 bootstraps were performed and only changes with probabilities
262 of >99% were considered.

263

264 **2.5 Source end-members mixing calculation**

265 The potential distal dust sources are discussed at a continental scale (e.g., Southern South
266 America and Southern Africa) because our initial mixing model attempts have shown that the
267 sources cannot be resolved on a sub-continental scale. Puna-Altiplano-Plateau, Central Western
268 Argentina and Patagonia were grouped together as the Southern South American dust source
269 end-member. Sua Pan and Etosha Pan were grouped as the Southern African end-member. The
270 contributions of different source end-members were calculated based on the method of ratio-
271 to-ratio relationships in the mixing balance described in Albarède, (1996) as equation 2:

$$272 \left(\frac{C^{i2}}{C^{i1}} \right)_{mix} = \frac{\sum_{j=1}^n C_j^{i2} f_j}{C_{mix}^{i1}} \quad (\text{Eq. 2})$$

273 Where C^{i1} and C^{i2} are the REE concentrations or Nd isotopes in a mixture of n components j
274 and represents each component (end-member). f is the fraction of component j in the mixed
275 dust depositing at AMS. Details on the calculation are reported in Table S5.

276

277 **3. Results**

278 **3.1. Core description**

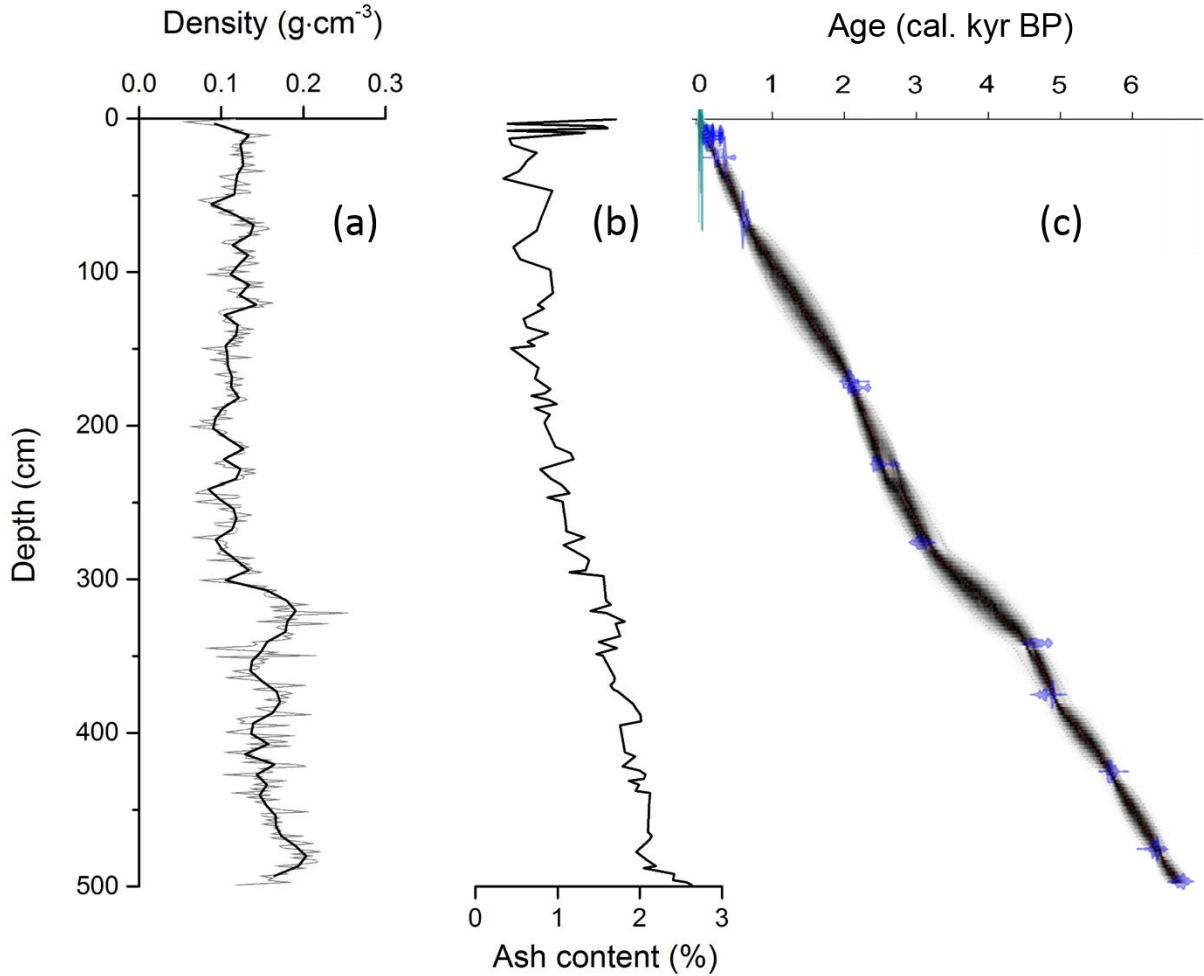
279 The total length of the core is 500 cm. Between 500 cm and 340 cm depth, a compacted, in
280 general relatively well-preserved peat deposit was formed. The peat is laminated, showing a cm-
281 scale alternation between fibrous well preserved *Sphagnum*-dominated layers and more

282 amorphous less well preserved layers. From 340 cm to 20 cm the peat becomes less compacted
283 showing different units of more or less well preserved peat, with visible plant macrofossils in
284 some parts. The top 20 cm of the core reflects the modern vegetation which consists mainly of
285 brown mosses together with some *Sphagnum* spp. (Fig. S3)

286

287 **3.2. Bulk density and ash content**

288 The density profile of the AMS peat core shows a general decreasing trend with an abrupt
289 drop at ~315 cm (Fig. 2a). From 500 cm to 315 cm, the median density is 0.17 g cm^{-3} ($0.08 - 0.26$
290 g cm^{-3}) with relatively higher values between 340 cm and 315 cm. From 315 cm upwards, the
291 density is lower with a median value of 0.12 g cm^{-3} ($0.05 - 0.16 \text{ g cm}^{-3}$). The ash content in the
292 AMS peat core mirrors partly the density profile and shows a general decreasing trend from
293 bottom to top (Fig. 2b), varying between 2.63% and 0.34%. The abrupt decrease between 340
294 cm and 315 cm present in the density profile is not as prominent in the ash content.



295
 296 Fig. 2. (a) Density (black line = for 5-point smoothing), (b) ash content and (c) age depth model (^{14}C in blue,
 297 ^{210}Pb Constant-Rate-Supply model in green) of the AMS peat core. For details on the top 50 cm chronology,
 298 we refer to Fig. S4 in supplementary information.

299

300 3.3. Geochronology

301 Radiocarbon and calibrated ages are shown in Table 1. The ^{210}Pb , ^{137}Cs and ^{241}Am results are
 302 published in Li et al., (2017). The ^{210}Pb Constant Rate Supply model is in good agreement with
 303 post-bomb ^{14}C ages. The age-depth model of the core was based on a combination of
 304 radiocarbon dating, post-bomb and ^{210}Pb dating (Fig. 2c; Fig. S4). The model shows that the peat
 305 sequence spans the last 6.6 kyr (Table S6), with a mean accumulation rate of 0.76 mm yr^{-1} .

306 Table 1. Radiocarbon dating results from Amsterdam Island peat sequence. Four samples were dated to a
 307 post-bomb period (Goodsite et al., 2001; Hua, 2009; Spalding et al., 2005) and the results calibrated using SH
 308 zone 1-2 calibration curve (Hua et al., 2013) by Calibomb software (Stuiver and Reimer, 2003). Other results
 309 were calibrated using the SHCal13 calibration curve (Hogg et al., 2013). Age-depth modelling was performed
 310 with Bacon, R routine (Blaauw and Christen, 2011).

Lab ID	Mid-Point Depth (cm)	Material dated	pMC*	Calibrated age (median)	Selected intervals (years BP)	calibrated
SacA50049	2.0	<i>Chorisondonti um/Dicranoloma</i> stems + leaves	107.18 ± 0.28		[-58 ; -53]	
SacA50050	3.5	Brown moss stems	120.36 ± 0.30		[-37 ; -35]	
SacA50051	4.9	Brown moss + liverworts stems	146.21 ± 0.32		[-24 ; -22]	
SacA50052	6.4	Brown moss + liverworts stems	116.81 ± 0.28		[-10 ; -10]	

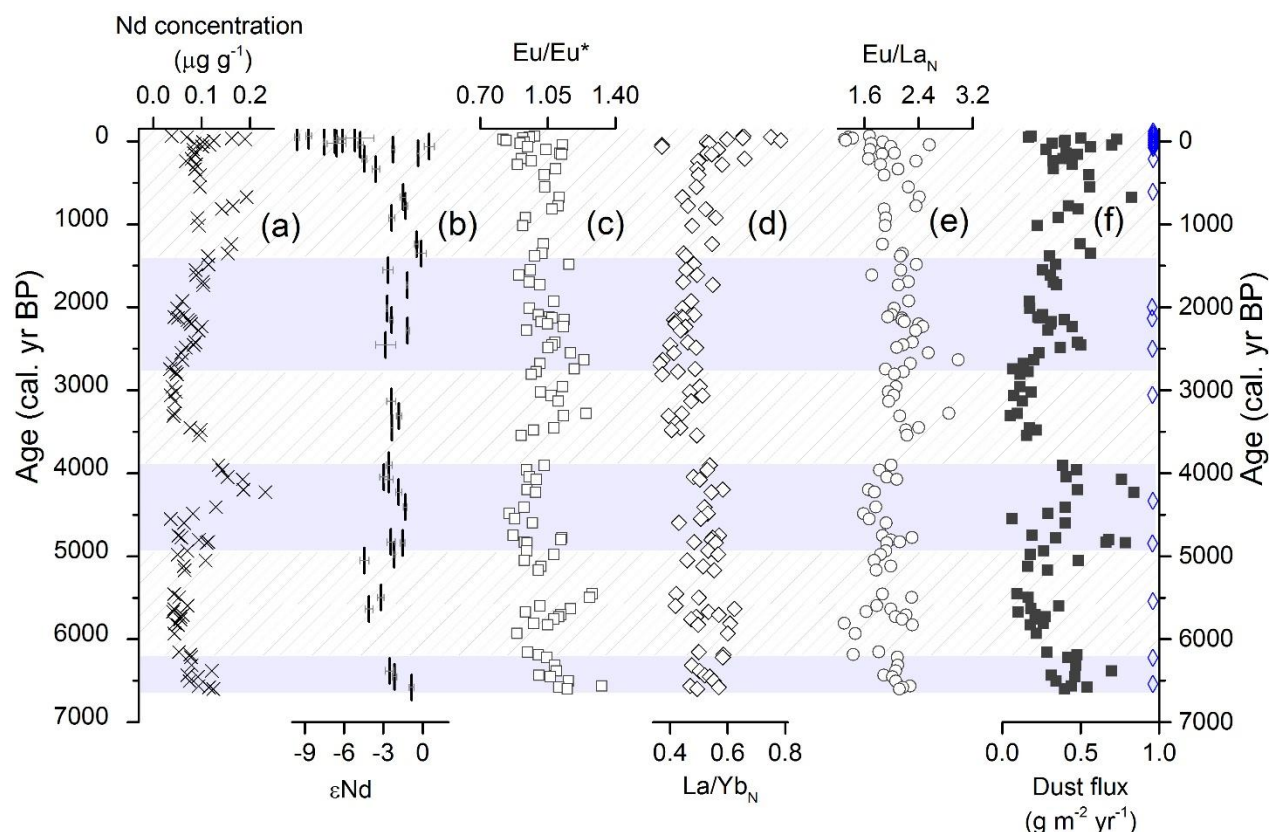
Lab ID	Mid-Point Depth (cm)	material	14C age (yr BP) ^a	Calibrated age (median)	Calibrated age range with 95.4% probability (BP)
SacA50053	7.8	Brown moss stems	135 ± 30	8	1 - 16
SacA50054	9.4	Brown moss stems	115 ± 30	26	14 - 39
SacA50055	10.8	Brown moss stems + leaves	80 ± 30	44	27 - 62
SacA50056	12.0	Brown moss stems + <i>Chorisondonti um/Dicranoloma</i> leaves	160 ± 30	57	33 - 96
SacA50057	13.2	Brown moss stems	70 ± 30	65	35 - 127
GdA-4136	24.9	brown moss stems	275 ± 25	198	150 - 310
GdA-4558	65.4	Residue (<i>Sphagnum</i> dominated)	595 ± 25	561	510 - 640
GdA-4560	170.7	Brown moss stems	2100 ± 25	2028	1920 - 2105
GdA-4137	174.8	Brown moss stems	2170 ± 30	2076	2005 - 2145
GdA-4138	224.4	Brown moss stems	2430 ± 30	2530	2365 - 2700
GdA-4139	275.4	Brown moss	2925 ± 30	3092	2930 - 3330

GdA-4561	340.9	stems Brown moss stems	4145 ± 35	4485	4225 - 4645
GdA-4140	374.4	<i>Sphagnum</i>	4285 ± 30	4850	4700 - 5025
GdA-4141	424.4	<i>Sphagnum</i> + brown moss	4960 ± 30	5630	5500 - 5745
GdA-4142	474.8	<i>Sphagnum</i> stems	5515 ± 35	6280	6140 - 6410
GdA-4143	495.9	<i>Sphagnum</i> stems	5860 ± 35	6565	6420 - 6700

311

312 **3.4. Peat REE and Nd isotopic signatures**

313 The concentration of the entire REE suite varies between 0.18 and $1.26 \mu\text{g g}^{-1}$ (Table S7). The
314 variations in the down core concentrations of fourteen REE elements (La, Ce, Pr, Nd, Sm, Eu, Gd,
315 Tb, Dy, Ho, Er, Tm, Yb and Lu) are similar to each other. The Nd concentration profile is plotted
316 as an example (Fig. 3a). The ϵNd signature at the bottom of the peat core is -0.8 ± 0.2 (2σ , $n=1$).
317 There is a general decreasing trend in ϵNd values between 6.6 - 5.4 cal. ky BP, followed by an
318 approximately three-fold increase at 4.4 - 3.9 cal. kyr BP. The lowest ϵNd values occur at 3.3 -
319 2.7 cal. kyr BP, after which the ϵNd fluctuates with an overall increasing trend since 2.7 cal. kyr
320 BP. The Holocene peat ϵNd profile is relatively constant centering at -2 ± 1.2 (1σ , $n=34$, Fig.
321 3b, Table S7), except for the last 100 years showing more distinct negative signatures with an
322 average value of -7 ± 1.5 (1σ , $n=7$).



323
 324 Fig. 3. Profiles of (a) Nd concentration ($\mu\text{g g}^{-1}$); (b) Epsilon Neodymium (ϵNd); (c) Eu/Eu^* ; (d) La/Yb_N ; (e)
 325 Eu/La_N ; and (f) REE-based dust flux ($\text{g m}^{-2} \text{yr}^{-1}$) in AMS peat core. Diamonds represent the ^{14}C dated peat
 326 layers (20 in total). The blue and white shading are the zones determined by change point analysis for AMS
 327 dust flux.

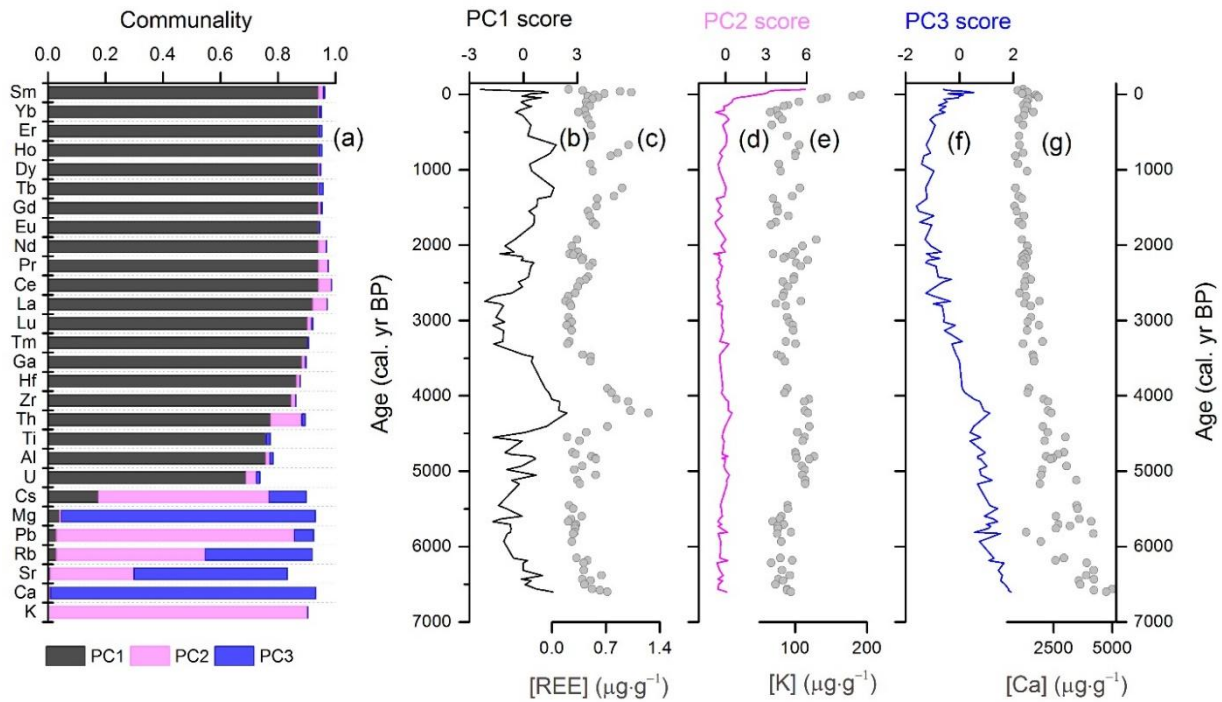
328
 329 REE ratios can be used for dust provenance-tracing. The Eu anomaly (Eu/Eu^*) was calculated
 330 with the equation $\text{Eu}/\text{Eu}^* = [\text{Eu}] / (([\text{Sm}] + [\text{Gd}]) / 2)$. The ratios of La/Yb_N and Eu/La_N have been
 331 normalized to Upper Continental Crust (Wedepohl, 1995). Peat average Eu/Eu^* , La/Yb_N and
 332 Eu/La_N values since the last 6.6 kyr are 1.03 ± 0.10 , 0.50 ± 0.07 and 2.01 ± 0.30 (1σ , $n=101$),
 333 respectively. The signatures of peat Eu/Eu^* , La/Yb_N and Eu/La_N remain relatively constant during
 334 the last 6.6 kyr (Fig. 3c, d, e), except for the last 100 years, which are characterized by an overall
 335 decreasing trend in Eu/Eu^* and Eu/La_N ratios, and an increasing trend in La/Yb_N ratio.

336

337 **4. Discussion**

338 **4.1. Elemental proxy interpretation**

339 The results of the PCA are reported in Fig. 4a and Fig. S5. The first component (PC1), explains 70%
340 of the total variance and consists of the entire REE suite and Ga, U, Th, Hf, Zr, Ti, Al (Fig. 4b, c),
341 which are known to be immobile and conservative elements. The second component (PC2),
342 accounts for 14% of the total variance and consists of K, Rb, Pb, and Cs (Fig. 4d, e). The
343 variability of this component is mainly driven by changes in the top part of the core, caused by
344 biological uptake and recycling by the surface moss vegetation (principally K, Rb and, to a lesser
345 extent Cs based on Fig. 4a) as well as anthropogenic Pb deposition (Damman, 1978; Shotyk,
346 1997). The third component (PC3), explains 12% of the total variance, and includes Sr, Ca and
347 Mg (Fig. 4f, g), which show higher values towards the bottom of the core (Shotyk, 1997).



348

349 Fig. 4. (a) Relative importance of each principal component (PC) for each chemical element; (b-g) PC scores (i.e.
350 transformed variable values for each sample) and their respective representative elements. All the
351 representative elements are shown as concentration ($\mu\text{g g}^{-1}$).

352 4.2. Dust deposition

353 The REE, also reflected by PC1, represent immobile and conservative elements. Therefore,
354 the mineral deposition rate (dust flux, $\text{g m}^2 \text{yr}^{-1}$) was calculated as equation 3:

$$355 \text{Dust flux}_i = \frac{\sum[\text{REE}]_i \times \text{peat vertical } AR_i \times \text{density}_i}{\sum[\text{REE}]_{UCC}} \times 10000 \quad (\text{Eq. 3})$$

356 Where $\sum[\text{REE}]_i$ is the sum of all REE concentrations ($\mu\text{g g}^{-1}$) in sample i , *peat vertical* AR_i
357 is the peat accumulation rate (cm yr^{-1}), obtained by *depth length* $_i$ /*age interval* $_i$, *density* $_i$ is
358 the density of the sample (g cm^{-3}), $\sum[\text{REE}]_{UCC}$ is the sum of the REE concentrations in the
359 upper continental crust (Wedepohl, 1995).

360

361 The dust flux profile shown in Fig.3, varies from $0.05 - 0.84 \text{ g m}^2 \text{yr}^{-1}$ with a median value of
362 $0.32 \text{ g m}^2 \text{yr}^{-1}$ (Fig. 3f). The REE-based AMS dust flux is comparable to the late Holocene ^{232}Th
363 reconstructed dust flux of $0.5 - 1.0 \text{ g m}^{-2} \text{yr}^{-1}$ over the Western Indian Ocean (Kienast et al.,
364 2016). Individual dust flux values are sensitive to spikes in REE concentration, to the ^{14}C age
365 model, and to the peat density. The highest dust fluxes are recorded between 4.2 cal. kyr BP and
366 4.8 cal. kyr BP, and are related to maxima in REE concentration and peat accumulation rate. We
367 applied a change-point analysis to identify changes in the probability distribution of the dust flux.
368 Four change-points with >99% confidence level, were identified: 6.2 cal. kyr BP; 4.9 cal. kyr BP;
369 3.9 cal. kyr BP; 2.7 cal. kyr BP and 1.4 cal. kyr BP. We therefore separate the dust flux profile into
370 six zones for discussion (see blue and white shading on Fig. 3, and section 4.4): (1) 6.6 - 6.2 cal.

371 kyr BP; (2) 6.2 - 4.9 cal.kyr BP; (3) 4.9 - 3.9 cal. kyr BP; (4) 3.9 - 2.7 cal. kyr BP; (5) 2.7 - 1.4 cal. kyr
372 BP; (6) 1.4 cal. kyr BP to the present (2014 AD).

373 The median ash content of 1.3% (n=101) in AMS peat core is low compared to the 2.9%
374 recorded in a peat core from Tierra del Fuego in Southern South America (Vanneste et al., 2016)
375 and 12.9% from a core in the Mfabeni peatland in Southern Africa (Humphries et al., 2017). The
376 low ash content suggests limited groundwater inputs, even in the deeper minerotrophic part of
377 the bog (detailed explanations for trophic status see Supplementary Information Text S4 and Fig.
378 S6).

379

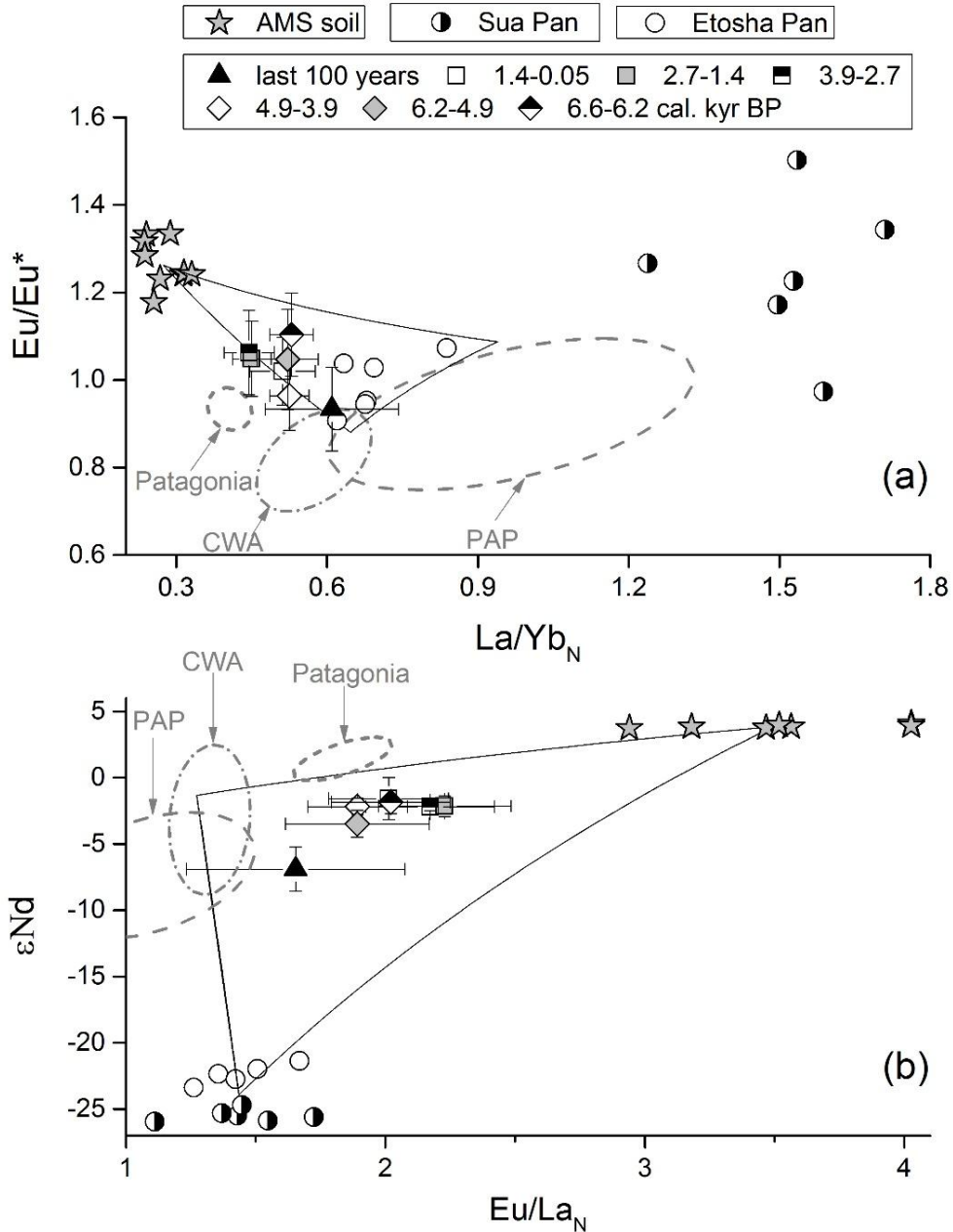
380 **4.3. Dust provenance**

381 Studies on atmospheric deposition at AMS, using ^{222}Rn , ^{210}Pb and air mass back trajectories
382 suggested some continental inputs to AMS, in particular from Southern Africa (Angot et al., 2014;
383 Gaudichet et al., 1989; Polian et al., 1986), and Southern South America (Fig. S2). Comparison of
384 ϵNd values in the AMS peat sequence with the reference datasets of the potential dust source
385 end-members (local, Southern Africa, and Southern South America) show that ϵNd values of the
386 peat samples lie between the local and continental dust sources (Fig. 5, Fig. S7). This also
387 suggests that AMS can potentially receive dust from local, Southern African, and Southern South
388 American sources.

389

390 The AMS soil samples display slightly higher Eu/Eu^* (median 1.24, Fig. 5) and lower $\text{La}/\text{Yb}_\text{N}$
391 ratios (median 0.27, Fig. 5) compared to the peat samples. The Southern African end-member

392 (including both Sua Pan and Etosha Pan) has Eu/Eu^* ratios that are close to those for the AMS
393 peat samples, but show higher La/Yb_N ratios (median 1.04). In comparison with the peat
394 samples, Eu/Eu^* ratios are relatively lower and La/Yb_N ratios are analogous in the Southern
395 American end-member (including Puna-Altiplano-Plateau, Central Western Argentina and
396 Patagonia, Gili et al., 2017). The average ϵNd value of the AMS soil samples is 3.9 ± 0.2 (2σ , $n = 7$,
397 Fig. 5b), much higher than those in the peat samples ($\epsilon\text{Nd} -9.6 - 0.5$). The Southern African end-
398 member has a more negative signature of -24 ± 1.7 (1σ , $n=11$, Fig. 5b). Both ϵNd (median 3.84)
399 and Eu/La_N (median 3.52) are higher in the local soils than in the Southern African end-member
400 (median $\epsilon\text{Nd} = -24.72$, median $\text{Eu}/\text{La}_N = 1.44$). The ϵNd signatures in the Southern South
401 American end-member overlap with those in the peat samples, while the Eu/La_N ratios are
402 relatively lower in the Southern South American end-member.



403
 404 Fig. 5. Relationships of La/Yb_N vs Eu/Eu^* (a), and Eu/La_N vs ϵNd (b) in AMS peat together with its Potential
 405 Source Areas (normalized to UCC, Wedepohl, 1995). Peat samples are shown as triangles/squares/diamonds,
 406 with different shapes representing different periods of the last 100 years (number of samples based on Fig. 5a,
 407 $n = 8$), 1.4 - 0.05 cal. kyr BP ($n = 17$), 2.7 - 1.4 cal. kyr BP ($n = 21$), 3.9 - 2.7 cal. kyr BP ($n = 13$), 4.9 - 3.9 cal. kyr
 408 BP ($n = 15$), 6.2 - 4.9 cal. kyr BP ($n = 17$), and 6.6 - 6.2 cal. kyr BP ($n = 10$), respectively. Black-edge stars: AMS
 409 soils; Half-open circles: dust/soil in Sua Pan; Open circles: dust/soil in Etosha Pan. Puna-Altiplano-Plateau (PAP,
 410 nine data points), Central Western Argentina (CWA, five data points) and Patagonia (11 data points) are
 411 shown in Ellipses (mean data with 95% confidence level, Gili et al., 2017); The black lines in (a) and (b)
 412 represent the End-member mixing lines among AMS soil, Southern Africa (Sua Pan + Etosha Pan) and

413 Southern South America (PAP + CWA + Patagonia) (see supplementary information Table S5 for detailed
 414 calculations, after Albarède, 1996).

415 Using the multi-proxy mixing model (Fig. 5), ϵNd and REE ratios indicate that the peat
 416 received approximately 40% of dust from local sources, 15% from Southern Africa and 45% from
 417 Southern South America. Dust source proportions were relatively constant over the last 6.6 kyr,
 418 except during the last 100 years (Table 2). Since 1910 AD, the model estimates a relative
 419 decrease in the local dust input (15%), while the relative contribution of Southern South Africa
 420 doubled (32%), with the Southern South American dust component (53%) showing little
 421 significant change.

422
 423 Table 2. The mean dust contributions of local, Southern African and Southern American dust to the AMS peat
 424 sampling site during the Holocene (kyr) and last 100 years. Estimates are based on a REE proxy mass balance
 425 model. Potential African and South American dust sources are lumped (see text). Uncertainty range
 426 corresponds to 1σ .

Time interval (kyr)	local	Southern Africa	Southern America
the last 100 years	15% (5%-25%)	32% (25%-40%)	53% (40%-65%)
1.4 -0.05	41% (35%-50%)	15% (10%-20%)	44% (30%-55%)
2.7-1.4	44% (35%-55%)	12% (5%-20%)	44% (30%-55%)
3.9-2.7	46% (40%-55%)	15% (10%-20%)	39% (25%-50%)
4.9-3.9	36% (30%-40%)	9% (5%-15%)	55% (40%-70%)
6.2-4.9	35% (25%-40%)	15% (5%-25%)	50% (35%-70%)
6.6-6.2	41% (35%-45%)	9% (5%-15%)	50% (45%-60%)

427
 428 In addition to an important local dust contribution (40%), likely from weathered basalt cliffs
 429 adjacent to the AMS peat bog, the mixing model indicates that from 6.6 kyr BP to 1910 AD,
 430 Southern South America is an important contributor of dust (45%; Table 2). The 14-day back
 431 trajectories show the air masses passing AMS that partially originate from Southern South
 432 America, covering the Puna-Altiplano-Plateau, Central Western Argentina and Patagonia (Fig.
 433 S2). This is also supported by modern dust observations. For example, combining
 434 ground/satellite observations and atmospheric modelling, Gaiero et al., (2013) found that large

435 dust storms at the Puna-Altiplano-Plateau (15° and 26°S) can be developed and injected into the
436 high-altitude subtropical jet stream of the SWW, which hence can be transported over long
437 distances (Gaiero, 2007). Dust from the Central Western Argentinean lowlands (between ~27°
438 and ~39°S), can also be uplifted by strong vertical air motion and be entrained into the SWW
439 (Gili et al., 2017). Once lifted into the troposphere, dust can be transported over thousands of
440 kilometers from its source area (Mahowald et al., 2005). Johnson et al., (2011) have shown that
441 Patagonian dust travels along the SWW pathways to the Southern Indian Ocean during dust
442 outbreak events in the austral summer, potentially reaching the Southern Indian Ocean in a
443 short period of time (days).

444
445 The mixing model also confirms a small (9 - 15%) but significant proportion of Southern
446 African dust through most of the Holocene (Table 2; Fig. 6). The Makgadikgadi Basin in
447 Botswana represented by our Sua Pan samples is the principal persistent dust source in
448 Southern Africa, with a general maximum dust emission activity in August-October (Prospero et
449 al., 2002). The prevailing winds in the area of Sua Pan (Fig. 1a) are tropical Easterlies that bring
450 moisture from the Indian Ocean (Bryant et al., 2007). Etosha Pan situated in the semi-north of
451 Namibia is a second principal Southern African dust source with prevailing northeasterly winds
452 (Vickery et al., 2013; Von Holdt et al., 2017). Both Sua Pan and Etosha Pan are characterized by a
453 proportion of northwesterly winds (Piketh, 2002; Von Holdt et al., 2017), confirming that dust
454 from Sua Pan and Etosha pan can be transported eastward into the Indian Ocean (Fig. S2).

455

456 **4.2 Lower dust input under equatorward-shifted/strengthened SWW**

457 The dust provenance mixing model showed that the relative proportion of dust contributions
458 from local, Southern African and Southern South American sources remained more or less
459 constant over the mid- to late Holocene at AMS. The estimated dust deposition flux ($\text{g m}^{-2} \text{yr}^{-1}$),
460 however, varied substantially on millennial timescales (Fig. 3a), likely resulting from changes in
461 the position and/or intensity of SWW. It is important to realize that a northward shift in SWW
462 may result in multiple antagonistic effects on dust: in dust source areas, an increase in SWW
463 strength may mobilize more dust. However, stronger SWW are characterized by more humid
464 conditions and more rainfall at least at the western to central sectors of the regions, leading to
465 denser vegetation and soil dust immobilization. Additionally, in the case of the high altitude
466 Puna-Altiplano-Plateau and Sua Pan/Etoshia Pan, the dust source areas do not directly lie within
467 the SWW belts, but their dust mobilizations can be influenced by SWW (see section 4.2). The net
468 effect of stronger SWW on dust emission therefore depends on local geography, meteorology
469 and vegetation (Marx et al., 2018). Studies on climate variability in AMS dust source areas
470 indicate enhanced dryness (e.g., relative higher dust availability) during 6.2 - 4.9 cal. kyr BP and
471 3.9 - 2.7 cal. kyr BP in both Puna-Altiplano-Plateau (Pueyo et al., 2011) and Southern Africa
472 (Chase et al., 2017; Chevalier and Chase, 2015; Cohen and Tyson, 1995; Cordova et al., 2017;
473 Nash et al., 2006). Dust mobilization in these source areas should therefore have been constant
474 or possibly enhanced during these two periods.

475
476 During periods of equatorward shifted and/or strengthened SWW potentially enhanced dust
477 mobilization will be subjected to more intense removal by rainfall and by turbulence via dry
478 deposition during transport (Miller et al., 1993; Moody et al., 1991). Evidence for this is based

479 on the relationship between rainfall chemistry and seasonal and inter-annual large-scale
480 atmospheric circulation patterns at AMS. (Moody et al., 1991) observed minima in rainfall anion
481 concentrations (non-sea salt Cl and SO₄, from continental origin) during austral winters,
482 characterized by stronger winds and enhanced precipitation. Distal dust records such as AMS,
483 thousands of kilometers away from dust sources, will overall tend to register decreased distal
484 dust deposition during stronger and/or equatorward shifted SWW due to the dominant effect of
485 dust removal during transport (Li et al., 2008). Stronger SWW with higher precipitation can
486 decrease local dust mobility by increasing local vegetation cover and humidity. We therefore
487 suggest that the AMS mineral dust flux minima from 6.2 - 4.9 cal. kyr BP and 3.9 - 2.7 cal. kyr BP
488 represent periods of equatorward shifted and/or strengthened SWW at this northern edge with
489 higher wind speed and enhanced precipitation over the dust transport trajectories, regardless of
490 the potential enhanced dust mobility at the source areas during these two periods. Conversely,
491 the three episodes of higher dust inputs (6.6 - 6.2 cal. kyr BP; 4.9- 3.9 cal. kyr BP; 1.4 cal. kyr BP
492 to present) represent periods of poleward-shifted and/or weakened SWW accompanied by
493 overall lower wind speeds and lower precipitation along the air mass trajectories from the
494 Southern Africa and Southern South America continents to AMS, together with relatively higher
495 local dust availability. The intermediate period from 2.7 - 1.4 cal. kyr BP (Fig. 3f), identified by
496 the change-point analysis, is a dust flux transition period characterized by gradual poleward
497 displacement of the SWW.

498
499 The timing and strength of the reconstructed environmental changes at AMS from 4.9 to 3.9
500 cal. kyr BP suggest these were part of a larger regional drought event, widely observed around

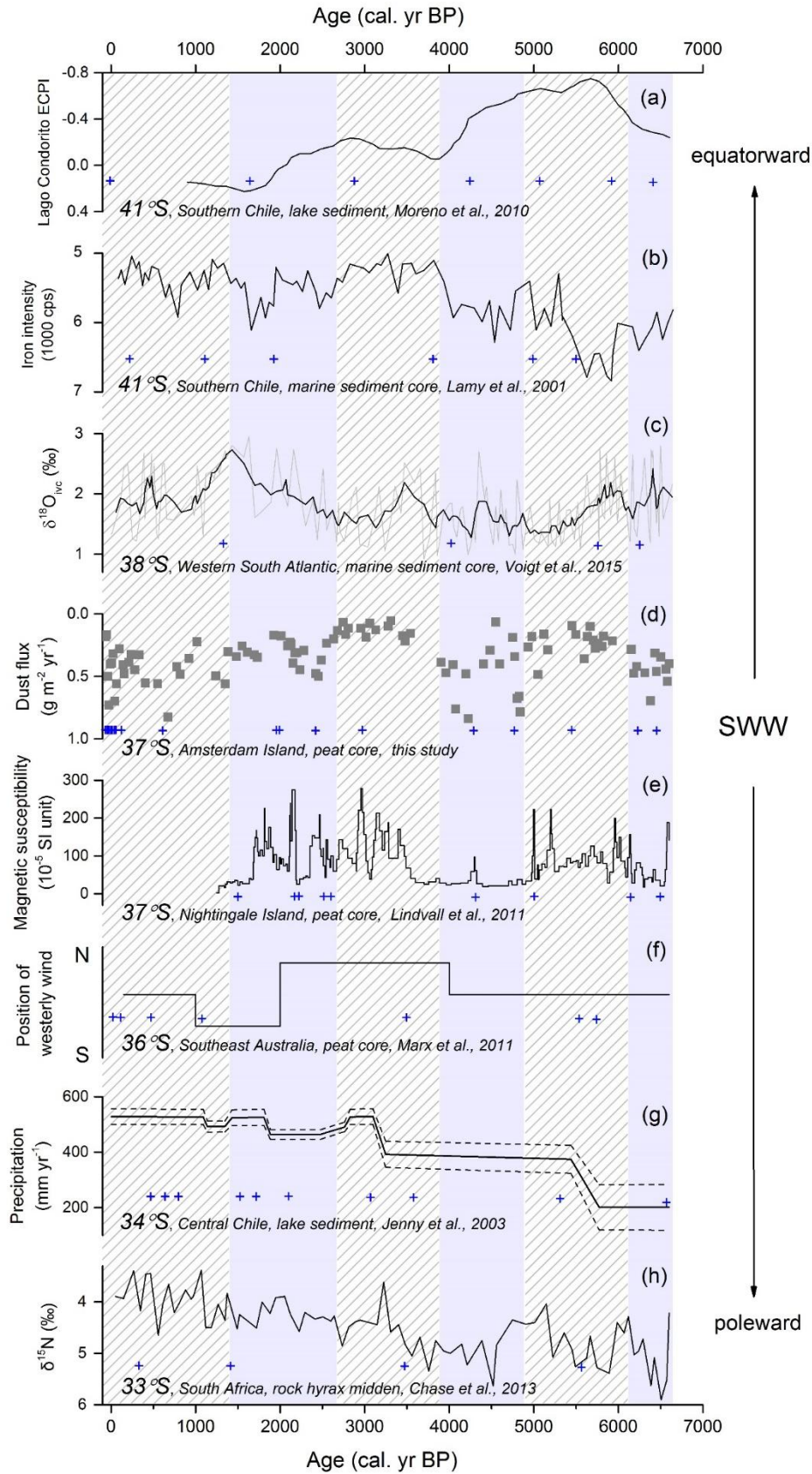
501 the Indian Ocean. For example, enhanced dry conditions have been found based on the abrupt
502 increased dust deposition in both Kilimanjaro ice cores (~4.0 cal. kyr BP, Thompson et al., 2002)
503 and in the Gulf of Oman marine sediment record (4.0 ± 0.1 cal. kyr BP, Cullen et al., 2000), based
504 on the positive sea surface salinity in a Northern Red Sea sediment core (~4.2 cal. kyr BP, Arz et
505 al., 2006), and based on the reduced annual rainfall evident in the Arabian sea sediment core
506 (~4.2 cal. kyr BP, Staubwasser et al., 2003). This mega-drought has potentially led to some of the
507 greatest societal upheavals in historical times (e.g., Egyptian Old Kingdom in the Nile Valley and
508 Akkadian Empire in Mesopotamia, Weiss, 2016). The severe dry conditions are explained by
509 changes in the monsoon system and extra-tropical airflow during winter (e.g., Cullen et al.,
510 2000; Staubwasser et al., 2003), which was suggested to follow variability in solar activity (Cullen
511 et al., 2000; Neff et al., 2001). Weaker SWW at AMS associated with the mega-drought event,
512 suggests a close teleconnection doi:10.1038/35077048 between SWW and other climate features
513 (e.g., monsoon system) in Indian Ocean sector around 4 cal. kyr BP.

514

515 We compare the AMS dust deposition record to other SH paleoclimate records from different
516 longitudes at the northern edge of SWW (33 - 41°S, Fig. 6). We find that the AMS dust flux (Fig.
517 6d) broadly anti-correlates with magnetic susceptibility in an oceanic minerotrophic peat core
518 from Nightingale Island (37°S, Fig. 6e, Lindvall et al., 2011). Magnetic susceptibility is a proxy for
519 surface runoff to this peat mire and therefore tracks rainfall in a very different manner to our
520 dust deposition proxy in the ombrotrophic AMS peat core (for explanations on trophic status
521 see supplementary Text S4). Both AMS and Nightingale cores suggest that the SWW moved
522 poleward at 4.9 - 3.9 cal. kyr BP, and equatorward at 6.2 - 4.9 cal. kyr BP and 3.9 - 2.7 cal. kyr BP.

523 Other published proxy records do not show coherent trends with these two SWW proxy records
524 over the past 6.6 kyr. For example, AMS dust flux, Nightingale Island magnetic susceptibility and
525 Southern Chile pollen composition (Moreno et al., 2010), indicate a poleward shift in SWW from
526 4.9 to 3.9 cal. kyr BP (Fig. 6a, d, e), where other records show no trend (Fig. 6c, g, h), or an
527 equatorward shift in SWW (Fig. 6b, f). Subsequently, during 3.9 - 2.7 cal. kyr BP period, the AMS
528 dust flux, Nightingale Island magnetic susceptibility (Lindvall et al., 2011), Southern Chilean
529 marine iron (Lamy et al., 2001), Central Chilean precipitation (Jenny et al., 2003), and South
530 African nitrogen isotope records (Chase et al., 2013) (Fig. 6d, e, b, g, h, respectively), suggest an
531 equatorward shift in SWW. Conversely the Chilean pollen (Moreno et al., 2010), Western South
532 Atlantic Oxygen isotope (Voigt et al., 2015) and Southeast Australian westerly position records
533 (Marx et al., 2011) (Fig 6a, c, f), show no change in SWW from 3.9 - 2.7 cal. kyr BP. We speculate
534 that the reasons for the observed variability in SWW proxy records are, 1/ the dependence of
535 SWW proxies on complex regional climate factors, and 2/ uncertainty in interpreting these
536 paleo-records due to dating uncertainties, and resolution and inherent complexity of proxies
537 used. A limitation of the AMS peat record is that it does not extend to the late glacial period,
538 where stronger trends in climate proxies have been previously detected (e.g., Kuhnt et al., 2015;
539 Lamy et al., 2010, see Fig. S8). The variations in SWW in the last 6.6 kyr that we infer from the
540 AMS dust record should therefore be regarded as moderate changes, compared to the
541 oscillations in SWW that have been associated with glacial/inter-glacial periods (e.g., De Deckker
542 et al., 2012; Van der Putten et al., 2015). Essentially, the ensemble of paleo-climate records
543 shown in Fig. 6, suggests that SWW are not homogeneous across at its northern zone (33 - 41°S)
544 over the last 6.6 kyr. More well-dated Holocene records using multiple proxies, and advanced

545 Earth system climate models are needed to understand the geographical variability in SWW
546 dynamics.



548 Fig. 6. Proxy records for wind position/strength at the northern SWW margin. (a) Pollen index *Eucryphia* +
549 *Caldcluvia/podocarps* (ECPI) from lake sediment core at Lago Condorito from Southern Chile (Moreno et al.,
550 2010); (b) Iron intensity from marine core Geob 3313-1 in Southern Chile (Lamy et al., 2001); (c) Ice volume
551 corrected *Globorotalia inflata* $\delta^{18}\text{O}$ ($\delta^{18}\text{O}_{\text{ivc}}$) from marine sediment Geob13862-1 in Western South Atlantic
552 (Voigt et al., 2015). Black line represents for the 5-point smoothing; (d) AMS mineral dust deposition from this
553 study; (e) Magnetic susceptibility from a peat core in Nightingale Island, Southern Atlantic (Lindvall et al.,
554 2011); (f) Shift in the position of SWW described in Marx et al., (2011); (g) Precipitation reconstruction from
555 Lake Aculeo in Central Chile (Jenny et al., 2003); (h) $\delta^{15}\text{N}$ -derived humidity from the hyrax middens
556 Seweweekspoort-1-5 in South Africa (Chase et al., 2013). The blue and white shading are the zones
557 determined by change point analysis for AMS dust flux. Crosses indicate ^{14}C dates.

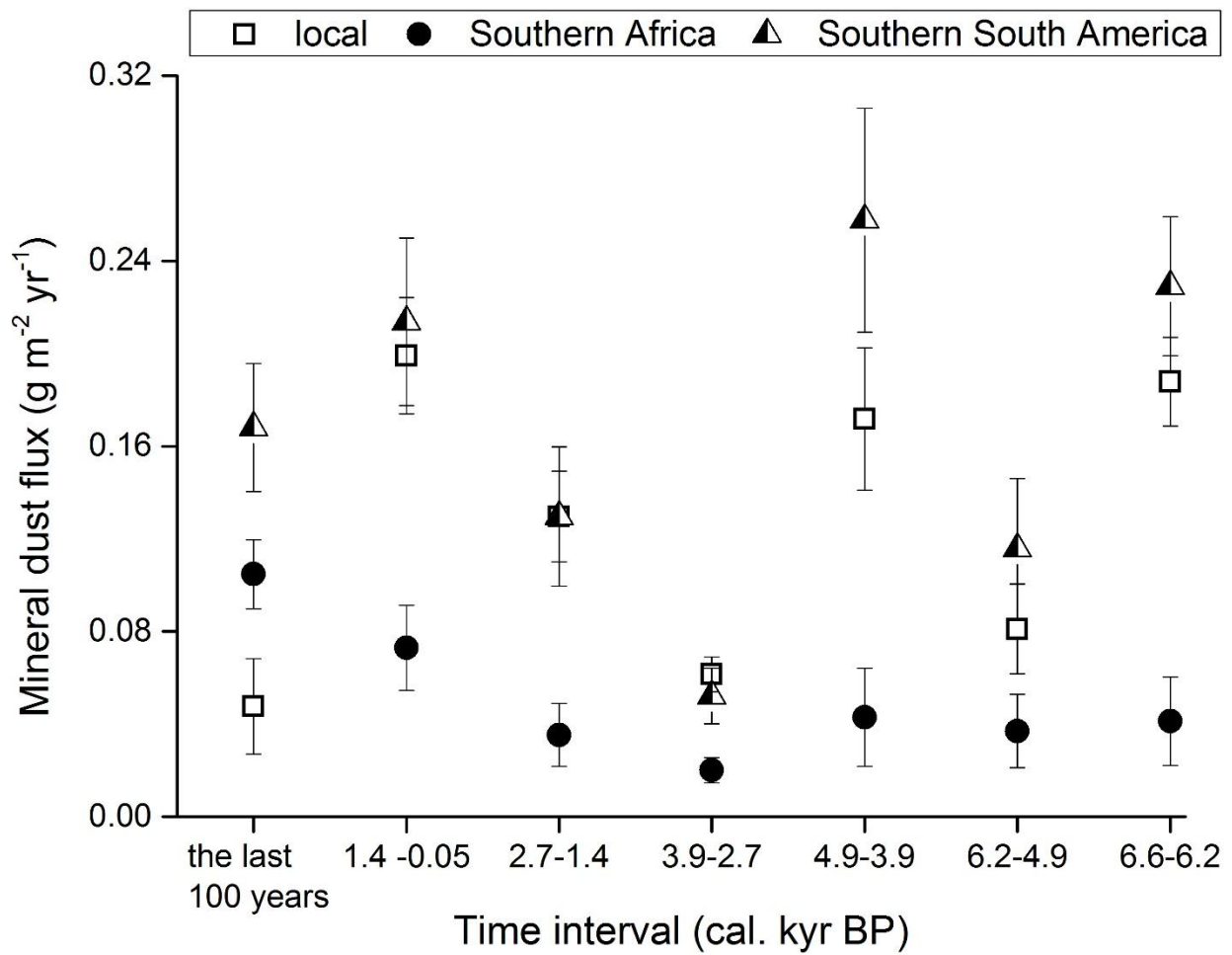
558

559 4.3 Climatic and anthropogenic influences in the last 100 years

560 The last 100 years (1910 - 2014 AD) display distinct REE and ϵNd signatures compared to the
561 rest of the core (Fig. 5; Fig. S9). This is accompanied by a quantitative increase in dust deposition
562 from Southern Africa (Fig. 7). The overall dust flux, however, is not significantly different during
563 the last 100 years compared to the 1.4 cal. kyr BP to present and 4.9 - 3.9 cal. kyr BP periods,
564 both characterized by relatively high dust flux and poleward position of the SWW. We therefore
565 suggest that other factors than the position of the SWW play a role in the recent shift in dust
566 provenance from Southern Africa. There is evidence of recent anthropogenic disturbances in the
567 Southern part of the African continent. For example, there is a major shift from grass-dominated
568 to sedge-dominated vegetation in the Okavango Delta (Northern Botswana) due to grazing and
569 fires (Nash et al., 2006). Remote sensing also clearly shows the effects of land clearing,
570 agriculture, and land degradation around Etosha Pan in Namibia (Strain and Engle, 1996). Land
571 degradation in recent years is also found in South Africa (Hoffman and Todd, 2000). These
572 changes to the local landscape enhance soil availability and erosion, thereby promoting a
573 relative increase of distal dust availability and subsequent inputs aligned along the prevailing
574 winds to AMS. Enhanced South African dust input to AMS during the past 100 years may

575 alternatively be caused by an overall drying trend over the South African continent as a
 576 response to human-climate interaction (IPCC, 2007). A general trend towards greater aridity and
 577 widespread drought in Southern Africa has indeed been recorded since the 19th century (e.g.,
 578 Kelso and Vogel, 2007; Nicholson, 2001; Nicholson et al., 2012; Riedel et al., 2012), supporting
 579 our findings.

580



581
 582 Fig. 7. The mineral dust contributions of local, Southern Africa and Southern South America ($\text{g m}^{-2} \text{yr}^{-1}$, 1σ)
 583 during different time intervals.

584

585 **5. Conclusions**

586 Understanding Holocene dust cycling and climate change in the Southern Hemisphere is
587 hampered by a paucity of high-resolution records in some sectors. We provide the first
588 Holocene mineral dust record from an Amsterdam Island peat core in the Southern Indian
589 Ocean. Southern South America and Southern Africa have been found to be the main distal dust
590 sources to AMS. Since 6.6 cal. kyr BP ago, except for the last 100 years, the dust inputs from
591 local, Southern South America and Southern Africa remained relatively constant, with the
592 former two as the main dust contributors. We interpret millennial scale shifts in dust deposition
593 rates to be caused by shifts in the SWW at AMS. A comparison of inferred SWW dynamics at
594 AMS to other Southern Hemisphere SWW proxy records at the northern edge of the wind belts
595 shows both similarities and differences, which suggests SWW were not zonally homogeneous
596 from mid to late Holocene (Lamy et al., 2019). In the last 100 years, the dust contribution from
597 Southern Africa doubles, possibly as a result of higher dust availability due to a drier climate,
598 and over-grazing, agriculture and land degradation by human influences. We suggest that
599 anthropogenic activities play an important role in the SH dust cycle during last 100 years.

600

601 **Acknowledgements:**

602 Many thanks for the support of the Mission 66 of Amsterdam Island, without which the field trip
603 could not be possible. We are grateful to Svante Björck, Bart Klink and Elisabeth Michel for the
604 peat sample coring. A very special thanks to Alain Quivoron and Hubert Launay for their
605 continuous directive and logistical support during and after fieldwork on Amsterdam Island.
606 Combined fieldwork was funded by the French Polar Institute (IPEV, Brest, France) through the
607 IPEV Programmes 1066 “PARAD” (to F. De Vleeschouwer) and 1065 PALATIO (to N. Van der

608 Putten and E. Michel). We are grateful to Nina Marchand (IPEV) for the logistical support, Cédric
609 Marteau for making the sampling possible in the protected areas of the TAAF Nature Reserve,
610 and Olivier Magand and Isabelle Jouvie for collecting the local soil samples. We thank the
611 members of the Dust Observations for Models (DO4) team for access to field samples from
612 southern Africa. We are grateful to Dominic Hodgson for his very helpful discussions and
613 comments on the draft. We thanks to Jan-Berend Stuut for the Australian samples (shown in
614 supplementary information) and his comments on the draft. We are grateful to Marie-José
615 Tavella, David Baqué, Camille Duquenoy, Aurélie Marquet, and Stéphanie Mounic for their help
616 with sample analysis. The additional radiocarbon ages were obtained as part of the Idex Peat3
617 project of the University of Toulouse and through the national service support: Artemis-INSU-
618 CNRS (to G. Le Roux). Chuxian Li's PhD is supported by a scholarship from the Chinese
619 Scholarship Council.

620

621 **References:**

- 622
- 623 Albarède, F., 1996. Introduction to geochemical modeling, 1. paperback ed. (with corr.). ed. Cambridge Univ.
624 Press, Cambridge, pp1-34.
- 625 Angot, H., Barret, M., Magand, O., Ramonet, M., Dommergue, A., 2014. A 2-year record of atmospheric
626 mercury species at a background Southern Hemisphere station on Amsterdam Island. *Atmos. Chem.*
627 *Phys.* 14, 11461–11473. <https://doi.org/10.5194/acp-14-11461-2014>
- 628 Appleby, P. G. "Chronostratigraphic techniques in recent sediments. In 'Tracking environmental change using
629 lake sediments. Volume 1: basin analysis, coring, and chronological techniques'.(Eds WM Last, JP
630 Smol) pp. 171–203." (2001).
- 631 Arz, H.W., Lamy, F., Pätzold, J., 2006. A Pronounced Dry Event Recorded Around 4.2 ka in Brine Sediments
632 from the Northern Red Sea. *Quat. res.* 66, 432–441. <https://doi.org/10.1016/j.yqres.2006.05.006>
- 633 Belokopytov, I. and Beresnevich, V. (1955) Giktorf's peat borers. *Torfyanaya Promyshlennost* 8, 9-10.
- 634 Betzer, P.R., Carder, K.L., Duce, R.A., Merrill, J.T., Tindale, N.W., Uematsu, M., Costello, D.K., Young, R.W.,
635 Feely, R.A., Breland, J.A., Bernstein, R.E., Greco, A.M., 1988. Long-range transport of giant mineral
636 aerosol particles. *Nature* 336, 568–571. <https://doi.org/10.1038/336568a0>
- 637 Blaauw, M., Christen, J.A., 2011. Flexible paleoclimate age-depth models using an autoregressive gamma
638 process. *Bayesian Anal.* 6, 457–474. <https://doi.org/10.1214/11-BA618>
- 639 Bryant, R.G., Bigg, G.R., Mahowald, N.M., Eckardt, F.D., Ross, S.G., 2007. Dust emission response to climate in
640 southern Africa. *J. Geophys. Res.* 112, D09207. <https://doi.org/10.1029/2005JD007025>
- 641 Castino, F., Bookhagen, B., Strecker, M.R., 2016. River-discharge dynamics in the Southern Central Andes and
642 the 1976-77 global climate shift: Discharge Dynamics in the Central Andes. *Geophys. Res. Lett.* 43,
643 11,679-11,687. <https://doi.org/10.1002/2016GL070868>
- 644 Chase, B.M., Boom, A., Carr, A.S., Meadows, M.E., Reimer, P.J., 2013. Holocene climate change in
645 southernmost South Africa: rock hyrax middens record shifts in the southern westerlies. *Quaternary*
646 *Science Reviews* 82, 199–205. <https://doi.org/10.1016/j.quascirev.2013.10.018>
- 647 Chase, B.M., Chevalier, M., Boom, A., Carr, A.S., 2017. The dynamic relationship between temperate and
648 tropical circulation systems across South Africa since the last glacial maximum. *Quaternary Science*
649 *Reviews* 174, 54–62. <https://doi.org/10.1016/j.quascirev.2017.08.011>
- 650 Chevalier, M., Chase, B.M., 2015. Southeast African records reveal a coherent shift from high- to low-latitude
651 forcing mechanisms along the east African margin across last glacial–interglacial transition.
652 *Quaternary Science Reviews* 125, 117–130. <https://doi.org/10.1016/j.quascirev.2015.07.009>
- 653 Cohen, A.L., Tyson, P.D., 1995. Sea-surface temperature fluctuations during the Holocene off the south coast
654 of Africa: implications for terrestrial climate and rainfall. *The Holocene* 5, 304–312.
655 <https://doi.org/10.1177/095968369500500305>
- 656 Cordova, C.E., Scott, L., Chase, B.M., Chevalier, M., 2017. Late Pleistocene-Holocene vegetation and climate
657 change in the Middle Kalahari, Lake Ngami, Botswana. *Quaternary Science Reviews* 171, 199–215.
658 <https://doi.org/10.1016/j.quascirev.2017.06.036>
- 659 Cullen, H. M., deMenocal, P. B., Hemming, S., Hemming, G., Brown, F. H., Guilderson, T., & Sirocko, F. (2000).
660 Climate change and the collapse of the Akkadian empire: Evidence from the deep sea. *Geology*, 28(4),
661 379-382.
- 662 Damman, A.W.H., 1978. Distribution and Movement of Elements in Ombrotrophic Peat Bogs. *Oikos* 30, 480.
663 <https://doi.org/10.2307/3543344>
- 664 De Deckker, P., Moros, M., Perner, K., Jansen, E., 2012. Influence of the tropics and southern westerlies on
665 glacial interhemispheric asymmetry. *Nature Geosci* 5, 266–269. <https://doi.org/10.1038/ngeo1431>
- 666 De Vleeschouwer, F., Chambers, F.M. and Swindles, G.T. (2010) Coring and sub-sampling of peatlands for
667 palaeoenvironmental research. *Mires and Peat* 7.
- 668 De Vleeschouwer, F., Vanneste, H., Mauquoy, D., Piotrowska, N., Torrejón, F., Roland, T., Stein, A., Le Roux, G.,
669 2014. Emissions from Pre-Hispanic Metallurgy in the South American Atmosphere. *PLoS ONE* 9,
670 e111315. <https://doi.org/10.1371/journal.pone.0111315>

671 Delqué-Količ, E., Caffy, I., Comby-Zerbino, C., Dumoulin, J.P., Hain, S., Massault, M., Moreau, C., Quiles, A.,
672 Setti, V., Souprayen, C., Tannau, J.F., Thellier, B., Vincent, J., 2013. Advances in Handling Small
673 Radiocarbon Samples at the Laboratoire de Mesure du Carbone 14 in Saclay, France. *Radiocarbon* 55,
674 648–656. <https://doi.org/10.1017/S0033822200057805>

675 Denton, G.H., Anderson, R.F., Toggweiler, J.R., Edwards, R.L., Schaefer, J.M., Putnam, A.E., 2010. The Last
676 Glacial Termination. *Science* 328, 1652–1656. <https://doi.org/10.1126/science.1184119>

677 Doucet, S., Giret, A., Weis, D. and Scoates, J., 2003. Géologie des îles Amsterdam et Saint Paul. *GEOLOGUES-*
678 *PARIS-*, pp.10-14.

679 Engelstaedter, S., Washington, R., 2007. Temporal controls on global dust emissions: The role of surface
680 gustiness: TEMPORAL CONTROLS. *Geophys. Res. Lett.* 34. <https://doi.org/10.1029/2007GL029971>

681 Fitchett, J.M., Mackay, A.W., Grab, S.W., Bamford, M.K., 2017. Holocene climatic variability indicated by a
682 multi-proxy record from southern Africa’s highest wetland. *The Holocene* 27, 638–650.
683 <https://doi.org/10.1177/0959683616670467>

684 Flatberg, I., Whinam, J., Lebouvier, M., 2011. Three species of Sphagnum endemic to Île Amsterdam, Terres
685 Australes et Antarctiques Françaises: *S. cavernulosum* sp. nov., *S. complanatum* sp. nov. and *S. islei*.
686 *Journal of Bryology* 33, 105–121. <https://doi.org/10.1179/1743282010Y.0000000019>

687 Fletcher, M.-S., Moreno, P.I., 2012. Have the Southern Westerlies changed in a zonally symmetric manner
688 over the last 14,000 years? A hemisphere-wide take on a controversial problem. *Quaternary*
689 *International* 253, 32–46. <https://doi.org/10.1016/j.quaint.2011.04.042>

690 Frenot, Y. and Valleix, T. (1990) Carte des sols de l'île Amsterdam (Terres Australes et Antarctiques Françaises),
691 Université, Station Biologique de Paimpont.

692 Frölicher, T.L., Sarmiento, J.L., Paynter, D.J., Dunne, J.P., Krasting, J.P., Winton, M., 2015. Dominance of the
693 Southern Ocean in Anthropogenic Carbon and Heat Uptake in CMIP5 Models. *J. Climate* 28, 862–886.
694 <https://doi.org/10.1175/JCLI-D-14-00117.1>

695 Frugone-Álvarez, M., Latorre, C., Giral, S., Polanco-Martínez, J., Bernárdez, P., Oliva-Urcia, B., Maldonado, A.,
696 Carrevedo, M.L., Moreno, A., Delgado Huertas, A., Prego, R., Barreiro-Lostres, F., Valero-Garcés, B.,
697 2017. A 7000-year high-resolution lake sediment record from coastal central Chile (Lago Vichuquén,
698 34°S): implications for past sea level and environmental variability: HIGH-RESOLUTION LAKE
699 SEDIMENT RECORD FROM CENTRAL CHILE. *J. Quaternary Sci.* 32, 830–844.
700 <https://doi.org/10.1002/jqs.2936>

701 Gaiero, D.M., 2007. Dust provenance in Antarctic ice during glacial periods: From where in southern South
702 America? *Geophys. Res. Lett.* 34, L17707. <https://doi.org/10.1029/2007GL030520>

703 Gaiero, D.M., Simonella, L., Gassó, S., Gili, S., Stein, A.F., Sosa, P., Becchio, R., Arce, J., Marelli, H., 2013.
704 Ground/satellite observations and atmospheric modeling of dust storms originating in the high Puna-
705 Altiplano deserts (South America): Implications for the interpretation of paleo-climatic archives: DUST
706 STORMS FROM PUNA-ALTIPLANO DESERTS. *J. Geophys. Res. Atmos.* 118, 3817–3831.
707 <https://doi.org/10.1002/jgrd.50036>

708 Gaudichet, A., Lefèvre, R., Gaudry, A., Ardouin, B., Lambert, G., Miller, J.M., 1989. Mineralogical composition
709 of aerosols at Amsterdam Island. *Tellus B* 41B, 344–352. <https://doi.org/10.1111/j.1600-0889.1989.tb00313.x>

711 Gili, S., Gaiero, D.M., Goldstein, S.L., Chemale, F., Jweda, J., Kaplan, M.R., Becchio, R.A., Koester, E., 2017.
712 Glacial/interglacial changes of Southern Hemisphere wind circulation from the geochemistry of South
713 American dust. *Earth and Planetary Science Letters* 469, 98–109.
714 <https://doi.org/10.1016/j.epsl.2017.04.007>

715 Givélet, N., Le Roux, G., Cheburkin, A., Chen, B., Frank, J., Goodsite, M.E., Kempter, H., Krachler, M.,
716 Noernberg, T., Rausch, N., Rheinberger, S., Roos-Barraclough, F., Sapkota, A., Scholz, C., Shotyk, W.,
717 2004. Suggested protocol for collecting, handling and preparing peat cores and peat samples for
718 physical, chemical, mineralogical and isotopic analyses. *J. Environ. Monit.* 6, 481–492.
719 <https://doi.org/10.1039/B401601G>

720 Goodsite, M.E., Rom, W., Heinemeier, J., Lange, T., Ooi, S., Appleby, P.G., Shotyk, W., van der Knaap, W.O.,
721 Lohse, C., Hansen, T.S., 2001. High-Resolution AMS 14 C Dating of Post-Bomb Peat Archives of
722 Atmospheric Pollutants. *Radiocarbon* 43, 495–515. <https://doi.org/10.1017/S003822200041163>
723 Hande, L.B., Siems, S.T., Manton, M.J., 2012. Observed Trends in Wind Speed over the Southern Ocean:
724 SOUTHERN OCEAN WIND TRENDS. *Geophys. Res. Lett.* 39, n/a-n/a.
725 <https://doi.org/10.1029/2012GL051734>
726 Hodgson, D.A., Sime, L.C., 2010. Southern westerlies and CO₂. *Nature Geosci* 3, 666–667.
727 <https://doi.org/10.1038/ngeo970>
728 Hogg, A.G., Hua, Q., Blackwell, P.G., Niu, M., Buck, C.E., Guilderson, T.P., Heaton, T.J., Palmer, J.G., Reimer, P.J.,
729 Reimer, R.W., Turney, C.S.M., Zimmerman, S.R.H., 2013. SHCal13 Southern Hemisphere Calibration,
730 0–50,000 Years cal BP. *Radiocarbon* 55, 1889–1903. https://doi.org/10.2458/azu_js_rc.55.16783
731 Hua, Q., 2009. Radiocarbon: A chronological tool for the recent past. *Quaternary Geochronology* 4, 378–390.
732 <https://doi.org/10.1016/j.quageo.2009.03.006>
733 Humphries, M.S., Benitez-Nelson, C.R., Bizimis, M., Finch, J.M., 2017. An aeolian sediment reconstruction of
734 regional wind intensity and links to larger scale climate variability since the last deglaciation from the
735 east coast of southern Africa. *Global and Planetary Change* 156, 59–67.
736 <https://doi.org/10.1016/j.gloplacha.2017.08.002>
737 Jacobsen, S.B., Wasserburg, G.J., 1980. Sm-Nd isotopic evolution of chondrites. *Earth and Planetary Science*
738 *Letters* 50, 139–155. [https://doi.org/10.1016/0012-821X\(80\)90125-9](https://doi.org/10.1016/0012-821X(80)90125-9)
739 Jenny, B., Wilhelm, D., Valero-Garcés, B., 2003. The Southern Westerlies in Central Chile: Holocene
740 precipitation estimates based on a water balance model for Laguna Aculeo (33° 50' S). *Climate*
741 *Dynamics* 20, 269 – 280. <https://doi.org/10.1007/s00382-002-0267-3>
742 Johnson, M.S., Meskhidze, N., Kiliyanpilakkil, V.P., Gassó, S., 2011. Understanding the transport of Patagonian
743 dust and its influence on marine biological activity in the South Atlantic Ocean. *Atmos. Chem. Phys.*
744 11, 2487–2502. <https://doi.org/10.5194/acp-11-2487-2011>
745 Kelso, C., Vogel, C., 2007. The climate of Namaqualand in the nineteenth century. *Climatic Change* 83, 357–
746 380. <https://doi.org/10.1007/s10584-007-9264-1>
747 Kienast, S.S., Winckler, G., Lippold, J., Albani, S., Mahowald, N.M., 2016. Tracing dust input to the global ocean
748 using thorium isotopes in marine sediments: ThoroMap. *Global Biogeochem. Cycles* 30,
749 1526–1541. <https://doi.org/10.1002/2016GB005408>
750 Killick, R., Eckley, I.A., Ewans, K., Jonathan, P., 2010. Detection of changes in variance of oceanographic time-
751 series using changepoint analysis. *Ocean Engineering* 37, 1120–1126.
752 <https://doi.org/10.1016/j.oceaneng.2010.04.009>
753 Kohfeld, K.E., Graham, R.M., de Boer, A.M., Sime, L.C., Wolff, E.W., Le Quéré, C., Bopp, L., 2013. Southern
754 Hemisphere westerly wind changes during the Last Glacial Maximum: paleo-data synthesis.
755 *Quaternary Science Reviews* 68, 76–95. <https://doi.org/10.1016/j.quascirev.2013.01.017>
756 Kuhnt, W., Holbourn, A., Xu, J., Opdyke, B., De Deckker, P., Röhl, U., Mudelsee, M., 2015. Southern
757 Hemisphere control on Australian monsoon variability during the late deglaciation and Holocene. *Nat*
758 *Commun* 6, 5916. <https://doi.org/10.1038/ncomms6916>
759 Lamy, F., Chiang, J.C.H., Martínez-Méndez, G., Thierens, M., Arz, H.W., Bosmans, J., Hebbeln, D., Lambert, F.,
760 Lembke-Jene, L., Stuut, J.-B., 2019. Precession modulation of the South Pacific westerly wind belt over
761 the past million years. *Proc Natl Acad Sci USA* 116, 23455–23460.
762 <https://doi.org/10.1073/pnas.1905847116>
763 Lamy, F., Hebbeln, D., Röhl, U., Wefer, G., 2001. Holocene rainfall variability in southern Chile: a marine record
764 of latitudinal shifts of the Southern Westerlies. *Earth and Planetary Science Letters* 185, 369–382.
765 [https://doi.org/10.1016/S0012-821X\(00\)00381-2](https://doi.org/10.1016/S0012-821X(00)00381-2)
766 Lamy, F., Kilian, R., Arz, H.W., Francois, J.-P., Kaiser, J., Prange, M., Steinke, T., 2010. Holocene changes in the
767 position and intensity of the southern westerly wind belt. *Nature Geosci* 3, 695–699.
768 <https://doi.org/10.1038/ngeo959>

769 Landschützer, P., Gruber, N., Haumann, F.A., Rödenbeck, C., Bakker, D.C.E., van Heuven, S., Hoppema, M.,
770 Metzl, N., Sweeney, C., Takahashi, T., Tilbrook, B., Wanninkhof, R., 2015. The reinvigoration of the
771 Southern Ocean carbon sink. *Science* 349, 1221–1224. <https://doi.org/10.1126/science.aab2620>
772 Lebouvier, M. and Frenot, Y., 2007. and Île Saint-Paul temperate. All have endemic species amongst their
773 biota. The Terres Australes et Antarctiques Françaises (TAAF) is. In *Papers and Proceedings of the*
774 *Royal Society of Tasmania* (Vol. 141, No. 1, p. 23). Royal Society of Tasmania.
775 Li, C., Le Roux, G., Sonke, J., van Beek, P., Souhaut, M., Van der Putten, N., De Vleeschouwer, F., 2017. Recent
776 ²¹⁰Pb, ¹³⁷Cs and ²⁴¹Am accumulation in an ombrotrophic peatland from Amsterdam Island
777 (Southern Indian Ocean). *Journal of Environmental Radioactivity* 175–176, 164–169.
778 <https://doi.org/10.1016/j.jenvrad.2017.05.004>
779 Li, F., Ginoux, P., Ramaswamy, V., 2008. Distribution, transport, and deposition of mineral dust in the
780 Southern Ocean and Antarctica: Contribution of major sources. *J. Geophys. Res.* 113, D10207.
781 <https://doi.org/10.1029/2007JD009190>
782 Lindvall, H., Björck, S., Holmgren, S., Ljung, K., Van der Putten, N., Porter, C., 2011. A Holocene peat record in
783 the central South Atlantic: an archive of precipitation changes. *GFF* 133, 195–206.
784 <https://doi.org/10.1080/11035897.2011.633708>
785 Ljung, K., Björck, S., 2007. Holocene climate and vegetation dynamics on Nightingale Island, South Atlantic—
786 an apparent interglacial bipolar seesaw in action? *Quaternary Science Reviews* 26, 3150–3166.
787 <https://doi.org/10.1016/j.quascirev.2007.08.003>
788 Lovenduski, N.S., Gruber, N., Doney, S.C., 2008. Toward a mechanistic understanding of the decadal trends in
789 the Southern Ocean carbon sink: SOUTHERN OCEAN CO₂ FLUX TRENDS. *Global Biogeochem. Cycles*
790 22, n/a-n/a. <https://doi.org/10.1029/2007GB003139>
791 Mahowald, N.M., Baker, A.R., Bergametti, G., Brooks, N., Duce, R.A., Jickells, T.D., Kubilay, N., Prospero, J.M.,
792 Tegen, I., 2005. Atmospheric global dust cycle and iron inputs to the ocean: ATMOSPHERIC IRON
793 DEPOSITION. *Global Biogeochem. Cycles* 19, n/a-n/a. <https://doi.org/10.1029/2004GB002402>
794 Marshall, G.J., Orr, A., van Lipzig, N.P.M., King, J.C., 2006. The Impact of a Changing Southern Hemisphere
795 Annular Mode on Antarctic Peninsula Summer Temperatures. *J. Climate* 19, 5388–5404.
796 <https://doi.org/10.1175/JCLI3844.1>
797 Marx, S.K., Kamber, B.S., McGowan, H.A., Denholm, J., 2011. Holocene dust deposition rates in Australia's
798 Murray-Darling Basin record the interplay between aridity and the position of the mid-latitude
799 westerlies. *Quaternary Science Reviews* 30, 3290–3305.
800 <https://doi.org/10.1016/j.quascirev.2011.07.015>
801 Marx, S.K., Kamber, B.S., McGowan, H.A., Petherick, L.M., McTainsh, G.H., Stromsoe, N., Hooper, J.N., May, J.-
802 H., 2018. Palaeo-dust records: A window to understanding past environments. *Global and Planetary*
803 *Change* 165, 13–43. <https://doi.org/10.1016/j.gloplacha.2018.03.001>
804 Marx, S.K., McGowan, H.A., Kamber, B.S., 2009. Long-range dust transport from eastern Australia: A proxy for
805 Holocene aridity and ENSO-type climate variability. *Earth and Planetary Science Letters* 282, 167–177.
806 <https://doi.org/10.1016/j.epsl.2009.03.013>
807 Miller, J.M., Moody, J.L., Harris, J.M., Gaudry, A., 1993. A 10-year trajectory flow climatology for Amsterdam
808 Island, 1980–1989. *Atmospheric Environment. Part A. General Topics* 27, 1909–1916.
809 [https://doi.org/10.1016/0960-1686\(93\)90296-B](https://doi.org/10.1016/0960-1686(93)90296-B)
810 Moody, J.L., Pszeny, A.A.P., Gaudry, A., Keene, W.C., Galloway, J.N., Polian, G., 1991. Precipitation
811 composition and its variability in the southern Indian Ocean: Amsterdam Island, 1980–1987. *J.*
812 *Geophys. Res.* 96, 20769. <https://doi.org/10.1029/91JD01921>
813 Moreau, C., Caffy, I., Comby, C., Delqué-Količ, E., Dumoulin, J.-P., Hain, S., Quiles, A., Setti, V., Souprayan, C.,
814 Thellier, B., Vincent, J., 2013. Research and Development of the Artemis 14 C AMS Facility: Status
815 Report. *Radiocarbon* 55, 331–337. <https://doi.org/10.1017/S0033822200057441>
816 Moreno, P.I., Francois, J.P., Moy, C.M., Villa-Martínez, R., 2010. Covariability of the Southern Westerlies and
817 atmospheric CO₂ during the Holocene. *Geology* 38, 727–730. <https://doi.org/10.1130/G30962.1>

818 Nash, D.J., Meadows, M.E., Gulliver, V.L., 2006. Holocene environmental change in the Okavango Panhandle,
819 northwest Botswana. *Quaternary Science Reviews* 25, 1302–1322.
820 <https://doi.org/10.1016/j.quascirev.2005.11.004>

821 Nicholson, S., 2001. Climatic and environmental change in Africa during the last two centuries. *Clim. Res.* 17,
822 123–144. <https://doi.org/10.3354/cr017123>

823 Nicholson, S.E., Dezfuli, A.K., Klotter, D., 2012. A Two-Century Precipitation Dataset for the Continent of Africa.
824 *Bull. Amer. Meteor. Soc.* 93, 1219–1231. <https://doi.org/10.1175/BAMS-D-11-00212.1>

825 Orsi, A.H., Whitworth, T., Nowlin, W.D., 1995. On the meridional extent and fronts of the Antarctic
826 Circumpolar Current. *Deep Sea Research Part I: Oceanographic Research Papers* 42, 641–673.
827 [https://doi.org/10.1016/0967-0637\(95\)00021-W](https://doi.org/10.1016/0967-0637(95)00021-W)

828 Parry, M.L., IPCC (Eds.), 2007. *Climate change 2007 - impacts, adaptation and vulnerability: contribution of*
829 *Working Group II to the Fourth Assessment Report of the Intergovernmental Panel on Climate*
830 *Change*, 1. publ. ed. Cambridge Univ. Press, Cambridge.

831 Piketh, S.J., 2002. Chemical evidence of long-range atmospheric transport over southern Africa. *J. Geophys.*
832 *Res.* 107, 4817. <https://doi.org/10.1029/2002JD002056>

833 Piotrowska, N., 2013. Status report of AMS sample preparation laboratory at GADAM Centre, Gliwice, Poland.
834 *Nuclear Instruments and Methods in Physics Research Section B: Beam Interactions with Materials*
835 *and Atoms* 294, 176–181. <https://doi.org/10.1016/j.nimb.2012.05.017>

836 Polian, G., Lambert, G., Ardouin, B., Jegou, A., 1986. Long-range transport of continental radon in subantarctic
837 and antarctic areas. *Tellus B: Chemical and Physical Meteorology* 38, 178–189.
838 <https://doi.org/10.3402/tellusb.v38i3-4.15126>

839 Prohaska, F. (1976) *The climate of argentina, Paraguay and Uruguay. Climates of Central and South America*
840 12, 13-112.

841 Prospero, J.M., Ginoux, P., Torres, O., Nicholson, S.E., Gill, T.E., 2002. Environmental characterization of global
842 sources of atmospheric soil dust identified with the NIMBUS 7 Total Ozone Mapping Spectrometer
843 (TOMS) absorbing aerosol product. *Rev. Geophys.* 40, 1002. <https://doi.org/10.1029/2000RG000095>

844 Pueyo, J.J., Sáez, A., Giralt, S., Valero-Garcés, B.L., Moreno, A., Bao, R., Schwab, A., Herrera, C., Klosowska, B.,
845 Taberner, C., 2011. Carbonate and organic matter sedimentation and isotopic signatures in Lake
846 Chungará, Chilean Altiplano, during the last 12.3kyr. *Palaeogeography, Palaeoclimatology,*
847 *Palaeoecology* 307, 339–355. <https://doi.org/10.1016/j.palaeo.2011.05.036>

848 Reid, P.C., Hari, R.E., Beaugrand, G., Livingstone, D.M., Marty, C., Straile, D., Barichivich, J., Goberville, E.,
849 Adrian, R., Aono, Y., Brown, R., Foster, J., Groisman, P., Hélaouët, P., Hsu, H.-H., Kirby, R., Knight, J.,
850 Kraberg, A., Li, J., Lo, T.-T., Myneni, R.B., North, R.P., Pounds, J.A., Sparks, T., Stübi, R., Tian, Y.,
851 Wiltshire, K.H., Xiao, D., Zhu, Z., 2016. Global impacts of the 1980s regime shift. *Glob Change Biol* 22,
852 682–703. <https://doi.org/10.1111/gcb.13106>

853 Revelle, 2019. *Procedures for Psychological, Psychometric, and Personality Research.* [https://personality-](https://personality-project.org/r/psych/)
854 [project.org/r/psych/](https://personality-project.org/r/psych/)

855 Riedel, F., Erhardt, S., Chauke, C., Kossler, A., Shemang, E., Tarasov, P., 2012. Evidence for a permanent lake in
856 Sua Pan (Kalahari, Botswana) during the early centuries of the last millennium indicated by
857 distribution of Baobab trees (*Adansonia digitata*) on “Kubu Island.” *Quaternary International* 253, 67–
858 73. <https://doi.org/10.1016/j.quaint.2011.02.040>

859 Sabine, C.L., 2004. The Oceanic Sink for Anthropogenic CO₂. *Science* 305, 367–371.
860 <https://doi.org/10.1126/science.1097403>

861 Saunders, K.M., Kamenik, C., Hodgson, D.A., Hunziker, S., Siffert, L., Fischer, D., Fujak, M., Gibson, J.A.E.,
862 Grosjean, M., 2012. Late Holocene changes in precipitation in northwest Tasmania and their potential
863 links to shifts in the Southern Hemisphere westerly winds. *Global and Planetary Change* 92–93, 82–91.
864 <https://doi.org/10.1016/j.gloplacha.2012.04.005>

865 Saunders, K.M., Roberts, S.J., Perren, B., Butz, C., Sime, L., Davies, S., Van Nieuwenhuyze, W., Grosjean, M.,
866 Hodgson, D.A., 2018. Holocene dynamics of the Southern Hemisphere westerly winds and possible
867 links to CO₂ outgassing. *Nature Geosci* 11, 650–655. <https://doi.org/10.1038/s41561-018-0186-5>

868 Shotyk, W., 1997. Atmospheric deposition and mass balance of major and trace elements in two oceanic peat
869 bog profiles, northern Scotland and the Shetland Islands. *Chemical Geology* 138, 55–72.
870 [https://doi.org/10.1016/S0009-2541\(96\)00172-6](https://doi.org/10.1016/S0009-2541(96)00172-6)

871 Shulmeister, J., 1999. Australasian evidence for mid-holocene climate change implies precessional control of
872 Walker Circulation in the Pacific. *Quaternary International* 57–58, 81–91.
873 [https://doi.org/10.1016/S1040-6182\(98\)00052-4](https://doi.org/10.1016/S1040-6182(98)00052-4)

874 Staubwasser, M., Sirocko, F., Grootes, P.M., Segl, M., 2003. Climate change at the 4.2 ka BP termination of the
875 Indus valley civilization and Holocene south Asian monsoon variability: SOUTH ASIAN HOLOCENE
876 CLIMATE CHANGE. *Geophys. Res. Lett.* 30. <https://doi.org/10.1029/2002GL016822>

877 Strain, P., and Engle, F. 1996. *Looking at Earth*. Turner, Atlanta, Ga, pp304.

878 Taylor, W. (2000a). Change-Point Analyzer 2.3 shareware program, Taylor Enterprises, Libertyville, Illinois.
879 Retrieved from <http://www.variation.com/cpa/>

880 Taylor, W. (2000b). Change-Point Analysis: A Powerful New Tool for Detecting Changes. Retrieved from
881 <http://www.variation.com/cpa/tech/changepoint.html>

882 Thompson, D.W.J., Solomon, S., 2002. Interpretation of Recent Southern Hemisphere Climate Change. *Science*
883 296, 895–899. <https://doi.org/10.1126/science.1069270>

884 Thompson, L.G., Mosley-Thompson, E., Davis, M.E., Henderson, K.A., Brecher, H.H., Zagorodnov, V.S.,
885 Mashiotta, T.A., Lin, P.-N., Mikhaleenko, V.N., Hardy, D.R., 2002. Kilimanjaro Ice Core Records:
886 Evidence of Holocene Climate Change in Tropical Africa. *Science* 298, 589–593.
887 <https://doi.org/10.1126/science.1073198>

888 Van der Putten, N., Hébrard, J.-P., Verbruggen, C., Van de Vijver, B., Disnar, J.-R., Spassov, S., de Beaulieu, J.-L.,
889 De Dapper, M., Keravis, D., Hus, J., Thouveny, N., Frenot, Y., 2008. An integrated
890 palaeoenvironmental investigation of a 6200 year old peat sequence from Ile de la Possession, Iles
891 Crozet, sub-Antarctica. *Palaeogeography, Palaeoclimatology, Palaeoecology* 270, 179–195.
892 <https://doi.org/10.1016/j.palaeo.2008.09.014>

893 Van der Putten, N., Mauquoy, D., Verbruggen, C., Björck, S., 2012. Subantarctic peatlands and their potential
894 as palaeoenvironmental and palaeoclimatic archives. *Quaternary International* 268, 65–76.
895 <https://doi.org/10.1016/j.quaint.2011.07.032>

896 Van der Putten, N., Verbruggen, C., Björck, S., Michel, E., Disnar, J.-R., Chapron, E., Moine, B.N., de Beaulieu,
897 J.-L., 2015. The Last Termination in the South Indian Ocean: A unique terrestrial record from
898 Kerguelen Islands (49°S) situated within the Southern Hemisphere westerly belt. *Quaternary Science*
899 *Reviews* 122, 142–157. <https://doi.org/10.1016/j.quascirev.2015.05.010>

900 Vanneste, H., De Vleeschouwer, F., Bertrand, S., Martínez-Cortizas, A., Vanderstraeten, A., Mattielli, N.,
901 Coronato, A., Piotrowska, N., Jeandel, C., Roux, G.L., 2016. Elevated dust deposition in Tierra del
902 Fuego (Chile) resulting from Neoglacial Darwin Cordillera glacier fluctuations: NEOGLACIAL ELEVATED
903 DUST DEPOSITION IN TIERRA DEL FUEGO. *J. Quaternary Sci.* 31, 713–722.
904 <https://doi.org/10.1002/jqs.2896>

905 Vanneste, H., De Vleeschouwer, F., Martínez-Cortizas, A., von Scheffer, C., Piotrowska, N., Coronato, A., Le
906 Roux, G., 2015. Late-glacial elevated dust deposition linked to westerly wind shifts in southern South
907 America. *Sci Rep* 5, 11670. <https://doi.org/10.1038/srep11670>

908 Varma, V., Prange, M., Lamy, F., Merkel, U., Schulz, M., 2011. Solar-forced shifts of the Southern Hemisphere
909 Westerlies during the Holocene. *Clim. Past* 7, 339–347. <https://doi.org/10.5194/cp-7-339-2011>

910 Varma, V., Prange, M., Merkel, U., Kleinen, T., Lohmann, G., Pfeiffer, M., Renssen, H., Wagner, A., Wagner, S.,
911 Schulz, M., 2012. Holocene evolution of the Southern Hemisphere westerly winds in transient
912 simulations with global climate models. *Clim. Past* 8, 391–402. <https://doi.org/10.5194/cp-8-391-2012>

913

914 Vickery, K.J., Eckardt, F.D., Bryant, R.G., 2013. A sub - basin scale dust plume source frequency inventory for
915 southern Africa, 2005 – 2008. *Geophys. Res. Lett.* 40, 5274 – 5279. <https://doi.org/10.1002/grl.50968>

916 Voigt, I., Chiessi, C.M., Prange, M., Mulitza, S., Groeneveld, J., Varma, V., Henrich, R., 2015. Holocene shifts of
917 the southern westerlies across the South Atlantic: Holocene shifts of Southern Westerlies.
918 *Paleoceanography* 30, 39–51. <https://doi.org/10.1002/2014PA002677>
919 Von Holdt, J.R., Eckardt, F.D., Wiggs, G.F.S., 2017. Landsat identifies aeolian dust emission dynamics at the
920 landform scale. *Remote Sensing of Environment* 198, 229–243.
921 <https://doi.org/10.1016/j.rse.2017.06.010>
922 Wedepohl, K.H. (1995) The composition of the continental crust. *Geochimica et Cosmochimica Acta* 59(7),
923 1217–1232.
924 Weiss, H., 2016. Global megadrought, societal collapse and resilience at 4.2–3.9 ka BP across the
925 Mediterranean and west Asia. *PAGES Mag* 24, 62–63. <https://doi.org/10.22498/pages.24.2.62>
926 Zickfeld, K., Fyfe, J.C., Saenko, O.A., Eby, M., Weaver, A.J., 2007. Response of the global carbon cycle to
927 human-induced changes in Southern Hemisphere winds. *Geophys. Res. Lett.* 34, L12712.
928 <https://doi.org/10.1029/2006GL028797>
929 nce 298, 589–593. <https://doi.org/10.1126/science.1073198>
930 Van der Putten, N., Hébrard, J.-P., Verbruggen, C., Van de Vijver, B., Disnar, J.-R., Spassov, S., de Beaulieu, J.-L.,
931 De Dapper, M., Keravis, D., Hus, J., Thouveny, N., Frenot, Y., 2008. An integrated
932 palaeoenvironmental investigation of a 6200 year old peat sequence from Ile de la Possession, Iles
933 Crozet, sub-Antarctica. *Palaeogeography, Palaeoclimatology, Palaeoecology* 270, 179–195.
934 <https://doi.org/10.1016/j.palaeo.2008.09.014>
935 Van der Putten, N., Mauquoy, D., Verbruggen, C., Björck, S., 2012. Subantarctic peatlands and their potential
936 as palaeoenvironmental and palaeoclimatic archives. *Quaternary International* 268, 65–76.
937 <https://doi.org/10.1016/j.quaint.2011.07.032>
938 Van der Putten, N., Verbruggen, C., Björck, S., Michel, E., Disnar, J.-R., Chapron, E., Moine, B.N., de Beaulieu,
939 J.-L., 2015. The Last Termination in the South Indian Ocean: A unique terrestrial record from
940 Kerguelen Islands (49°S) situated within the Southern Hemisphere westerly belt. *Quaternary Science*
941 *Reviews* 122, 142–157. <https://doi.org/10.1016/j.quascirev.2015.05.010>
942 Vanneste, H., De Vleeschouwer, F., Bertrand, S., Martínez-Cortizas, A., Vanderstraeten, A., Mattielli, N.,
943 Coronato, A., Piotrowska, N., Jeandel, C., Roux, G.L., 2016. Elevated dust deposition in Tierra del
944 Fuego (Chile) resulting from Neoglacial Darwin Cordillera glacier fluctuations: NEOGLACIAL ELEVATED
945 DUST DEPOSITION IN TIERRA DEL FUEGO. *J. Quaternary Sci.* 31, 713–722.
946 <https://doi.org/10.1002/jqs.2896>
947 Vanneste, H., De Vleeschouwer, F., Martínez-Cortizas, A., von Scheffer, C., Piotrowska, N., Coronato, A., Le
948 Roux, G., 2015. Late-glacial elevated dust deposition linked to westerly wind shifts in southern South
949 America. *Sci Rep* 5, 11670. <https://doi.org/10.1038/srep11670>
950 Varma, V., Prange, M., Lamy, F., Merkel, U., Schulz, M., 2011. Solar-forced shifts of the Southern Hemisphere
951 Westerlies during the Holocene. *Clim. Past* 7, 339–347. <https://doi.org/10.5194/cp-7-339-2011>
952 Varma, V., Prange, M., Merkel, U., Kleinen, T., Lohmann, G., Pfeiffer, M., Renssen, H., Wagner, A., Wagner, S.,
953 Schulz, M., 2012. Holocene evolution of the Southern Hemisphere westerly winds in transient
954 simulations with global climate models. *Clim. Past* 8, 391–402. <https://doi.org/10.5194/cp-8-391-2012>
955
956 Vickery, K.J., Eckardt, F.D., Bryant, R.G., 2013. A sub-basin scale dust plume source frequency inventory for
957 southern Africa, 2005–2008. *Geophys. Res. Lett.* 40, 5274–5279. <https://doi.org/10.1002/grl.50968>
958 Voigt, I., Chiessi, C.M., Prange, M., Mulitza, S., Groeneveld, J., Varma, V., Henrich, R., 2015. Holocene shifts of
959 the southern westerlies across the South Atlantic: Holocene shifts of Southern Westerlies.
960 *Paleoceanography* 30, 39–51. <https://doi.org/10.1002/2014PA002677>
961 Von Holdt, J.R., Eckardt, F.D., Wiggs, G.F.S., 2017. Landsat identifies aeolian dust emission dynamics at the
962 landform scale. *Remote Sensing of Environment* 198, 229–243.
963 <https://doi.org/10.1016/j.rse.2017.06.010>
964 Wedepohl, K.H. (1995) The composition of the continental crust. *Geochimica et Cosmochimica Acta* 59(7),
965 1217–1232.

966 Weiss, H., 2016. Global megadrought, societal collapse and resilience at 4.2-3.9 ka BP across the
967 Mediterranean and west Asia. *PAGES Mag* 24, 62–63. <https://doi.org/10.22498/pages.24.2.62>
968 Zickfeld, K., Fyfe, J.C., Saenko, O.A., Eby, M., Weaver, A.J., 2007. Response of the global carbon cycle to
969 human-induced changes in Southern Hemisphere winds. *Geophys. Res. Lett.* 34, L12712.
970 <https://doi.org/10.1029/2006GL028797>